The Contribution of Compressional Magnetic Pumping to the Energization of the Earth's Outer Electron Radiation Belt during High-Speed-Stream-Driven Storms

Joseph E. Borovsky[1,2] , Richard B. Horne[3], and Nigel P. Meredith[3]

[1] CLASP, University of Michigan, Ann Arbor, Michigan, USA
[2] Space Science Institute, Boulder, Colorado, USA
[3] British Antarctic Survey, Cambridge, England

Compressional magnetic pumping is an interaction between cyclic magnetic compressions and pitch-angle scattering with the scattering acting as a catalyst to allow the cyclic compressions to energize particles. Compressional magnetic pumping of the outer electron radiation belt at geosynchronous orbit in the dayside magnetosphere is analyzed by means of computer simulations, wherein solar-wind compressions of the dayside magnetosphere energize electrons with electron pitch-angle scattering by chorus waves and by EMIC. The magnetic pumping is found to produce a weak bulk heating of the electron radiation belt, and it also produces an energetic tail on the electron energy distribution. The amount of energization depends on the robustness of the solar-wind compressions and on the amplitude of the chorus and/or EMIC waves. Chorus-catalyzed pumping is better at energizing medium-energy (50 - 200 keV) electrons than it is at energizing higher energy electrons; at high energies (500 keV - 2 MeV) EMIC-catalyzed pumping is a stronger energizer. The magnetic-pumping simulation results are compared with energy-diffusion calculations for chorus waves in the dayside magnetosphere; in general compressional magnetic pumping is found to be weaker at accelerating electrons than is chorus-driven energy diffusion. In circumstances when solar-wind compressions are robust and when EMIC waves are present in the dayside magnetosphere without the presence of chorus, EMIC-catalyzed magnetic pumping could be the dominant energization mechanism in the dayside magnetosphere, but at such times loss-cone losses will be strong.

This is the author manuscript accepted for publication and has undergone full peer review but has not been through the copyediting, typesetting, pagination and proofreading process, which may lead to differences between this version and the Version of Record. Please cite this article as doi: 10.1002/2017JA024607

1. Introduction

Electrons in the Earth's outer radiation belt are energized during high-speed-stream-driven geomagnetic storms to relativistic energies [*Paulikas and Blake*, 1976; *Borovsky and Denton*, 2006]. Several mechanisms are thought to play a role in this heating, including (a) cyclotron resonance with whistler-mode chorus waves [*Summers et al.*, 1998; *Horne et al.*, 2005a, 2006], (b) ULF-induced radial diffusion [*Mathie and Mann*, 2001; *Tu et al.*, 2012], (c) drift resonance with ULF waves [*Elkington et al.*, 1999, 2003; *Sauvaud et al.*, 2013], and (d) substorm field collapse [*Kim et al.*, 2000; *Fok et al.*, 2001; *Dai et al.*, 2014].

The occurrence rate of substorms is high during high-speed-stream-driven storms [*Borovsky and Yakymenko*, 2017]. This leads to repeated injections of electrons with energies up to a few hundred keV into the inner magnetosphere [e.g., *Meredith et al.*, 2011; *Borovsky and Denton*, 2011; *Denton and Borovsky*, 2012] resulting in whistler-mode chorus wave activity [*Meredith et al.*, 2001, 2002, 2012; *Min et al.*, 2010]. Chorus waves accelerate seed electrons, with initial energies of a few hundred keV, up to MeV energies [*Horne et al.*, 2005a; 2005b; *Thorne et al.*, 2013], while at the same time leading to loss of lower-energy electrons [*Horne et al.*, 2005a; *Artemyev et al.*, 2015; *Albert et al.*, 2017].

Intense levels of radiation-belt electrons have been statistically linked to the amplitudes of low-frequency magnetic-field fluctuations in the magnetosphere [*Rostoker et al.*, 1998; *Mathie and Mann*, 2000; *Kozyreva et al.*, 2007; *Romanova and Pilipenko*, 2009] (although radiation-belt correlations with other parameters such as geomagnetic activity, solar-wind speed, and solar-wind number density are higher [*Borovsky and Denton*, 2010b; *Balikhin et al., 2011*; *Boynton et al.*, 2013; *Borovsky and Denton*, 2014; *Borovsky*, 2017]). Magnetic-field fluctuations in the magnetosphere are found to persist throughout the long durations of high-speed-stream-driven storms [*Borovsky and Denton*, 2010a], including compressive fluctuations [*Borovsky and Denton*, 2013; *Denton and Borovsky*, 2017]. ULF waves in the magnetosphere are known to be produced by the buffeting of the magnetosphere by variations in

the solar-wind dynamic pressure [*Mathie and Mann*, 2001; *Borovsky and Denton*, 2016]. Radial diffusion [*Falthammar and Walt*, 1969; *Ozeke et al.*, 2012] and drift-resonant acceleration [*Elkington et al.*, 1999, 2003; *Degeling et al.*, 2008] are two well-studied mechanisms by which magnetospheric ULF waves can affect the evolution of the electron radiation belt. It has been argued that the temporal compressions of the dayside magnetosphere by temporal variations of the solar-wind dynamic pressure can lead to collisional magnetic pumping of the radiation-belt electrons when pitch-angle scattering by plasma waves is present [*Liu et al.*, 1999; *Borovsky and Denton*, 2016].

Magnetic pumping is a consequence of two simultaneous processes: (1) cyclic magnetic compressions and (2) pitch-angle scattering. In the Earth's dayside magnetosphere compression occurs because of the temporal variations in the solar-wind ram pressure [*Wing and Sibeck*, 1997; *Kepko and Spence*, 2003; *Viall et al.*, 2009; *Borovsky and Denton*, 2010a, 2016; *Li et al.*, 2013]. For radiation-belt electrons in the dayside magnetosphere, pitch-angle scattering is believed to be produced by whistler-mode chorus outside of the plasmasphere [*Thorne et al.*, 2005; *Shprits et al.*, 2007], by electromagnetic ion-cyclotron waves inside and outside the plasmaspheric drainage plume [*Kovalevskiy*, 1980, 1981; *Jordanova et al.*, 2006; *Thorne et al.*, 2006; *Spasojevic and Fuselier*, 2009], and by whistler-mode hiss [*Chan and Holzer*, 1976; *Summers et al.*, 2008] inside the plasmaspheric drainage plume and the plasmasphere.

In this study the role of compressions of the dayside magnetosphere on the energization of the electron radiation belt is investigated. Specifically, the role of compressions with timescales slower than ULF periods is examined; these compressions are owed to temporal changes in the ram pressure of the solar wind caused by structure in the solar-wind plasma advecting past the Earth [*Borovsky and Denton*, 2016]. (Dayside compressions might also be caused by foreshock transients upstream of the Earth [e.g. *Safrankova et al.*, 2012; Hartinger et al., 2013].) These compressions are not periodic in time, but are irregular. In the magnetic-pumping process the energy for the energization of radiation-belt electrons comes from the solar-wind

compressions.

In this report computer simulations of the magnetic-pumping process will be driven by spacecraft measurements of magnetic-field compressions in the dayside magnetosphere during high-speed-stream-driven storms. The time-dependent magnetic-field strength B(t) that a particle experiences in the nightside magnetosphere is too difficult to estimate (cf. Sect. 6 of *Borovsky and Denton* [2016]); measured values of the changes in the magnetic-field strength ΔB are very large at geosynchronous orbit in the nightside [*Borovsky and Denton*, 2010a] and some of the time variation of the field strength is owed to the movement of gradients in the magnetic-field morphology at the dipole-tail transition. Hence, in this report the focus will be on the compressional magnetic pumping of radiation-belt electrons in the dayside magnetosphere.

The objective of this simulation study is to assess the contribution of magnetic pumping to the energization of the outer electron radiation belt, especially in comparison with chorus energy diffusion. To accomplish this the simulations will be kept simple and focused on magnetic pumping and on energy diffusion. Among the processes that will not be included in the simulations are (1) radial diffusion by ULF waves, (2) radial diffusion by the combined action of shell splitting and pitch-angle scattering, (3) time-dependence in the amplitudes of whistler-mode chorus waves and EMIC waves, (4) the time dependence of the substorm-injected electron population at 10 s to 100 s of keV, and (5) strongly increased electron loss due to combined effects of EMIC and chorus waves, even if these waves occur at different MLTs [e.g., *Mourenas et al.*, 2016].

This study is organized as follows. In Section 2 the magnetic-pumping process is explained. In Section 3 the computational methods that are used to simulate magnetic pumping are discussed along with the magnetic-field compressions used as input to the simulations (Section 3.1) and the values taken for pitch-angle-diffusion coefficients (Section 3.2) for whistler-mode chorus waves and for EMIC waves. In Section 4 the simulation results are discussed for initial-value-problem simulations (no fixed seed population) in Section 4.1

and for boundary-value problem simulations (with a constant seed population) in section 4.2. In Section 5 the simulation results for magnetic pumping are compared with energy diffusion for whistler-mode chorus. Section 6 contains discussions about the efficiency of magnetic pumping for energizing the outer electron radiation belt, about the action of magnetic pumping during CME-sheath-driven storms, and about the magnetic pumping of the outer proton radiation belt. The findings of this study are summarized in Section 7.

2. Compressional Magnetic Pumping

Magnetic pumping [*Alfven*, 1950; *Spitzer and Witten*, 1953; *Schluter*, 1957] is an interplay between cyclic magnetic compressions and pitch-angle scattering. In the absence of scattering, charged particles behave adiabatically in the cyclic compressions and no net particle energization occurs. Pitch-angle scattering breaks the adiabaticity of the particles and allows the cyclic compressions to systematically heat the particles. If the two processes occur simultaneously then some degree of heating is unavoidable. Basic explanations of the magnetic-pumping process can be found in *Alfven and Falthammar* [1963] and *Borovsky* [1986]. Magnetic pumping has been invoked to explain the heating of ions and electrons in the rapidly rotating magnetosphere of Jupiter [*Goertz,* 1978; *Borovsky et al.*, 1981; *Mu*, 1993], and to contribute to the energization of particles in the Earth's magnetosphere [*Alfven*, 1959; *Liu and Rostoker*, 1995; *Liu et al.*, 1999; *Dmitriev et al.*, 2001].

Note that the term "magnetic pumping" is also used in plasma physics to denote transit-time processes [e.g. *Koechlin and Samain*, 1971; *Canobbio*, 1972; *Tataronis and Grossmann*, 1976; *Kuijpers et al.*, 1997]: to avoid confusion in this report the term "compressional magnetic pumping" will be used. Compressional magnetic pumping has also been denoted as "collisional magnetic pumping" and as the "gyro-relaxation effect".

The energization timescale for compressional magnetic pumping depends on three parameters: (1) $\Delta B/B$ the fractional strength of the magnetic compression, (2) $\tau_{\rm cycle}$ the cycle time of the compression, and (3) $\tau_{\rm scat}$ the pitch-angle scattering timescale. Applying magnetic pumping to electrons in the dayside magnetosphere will involve compression-cycle times $\tau_{\rm cycle}$ in the range of 5 - 20 min, pitch-angle scattering times $\tau_{\rm scat}$ in the range of 10 - 1000 min, and compression amplitudes $\Delta B/B$ in the range of 0.05 - 0.2.

Analysis in the literature demonstrate that magnetic pumping will heat (i.e. increase the average kinetic energy) of a population of particles [e.g. *Alfven*, 1954; *Murty and Varma*, 1958]. Through the randomness of the pitch-angle scattering process, magnetic pumping also results in a momentum

diffusion (energy diffusion) of the particle population [cf. *Melrose*, 1969; *Borovsky et al.*, 1981; *Borovsky*, 1986, 1988; *Liu et al.*, 1999], which results in the rapid production of a high-energy tail on the distribution of particles.

3. Simulation Methods

The magnetic-pumping simulations follow the evolution in momentum p versus equatorial pitch angle α space of all of the electrons in a magnetic flux tube in the dayside magnetosphere. Electrons of different kinetic energies cross the dayside magnetosphere at different azimuthal speeds and a given set of electrons with diverse kinetic energies will not stay in the same flux tube. However, as electrons of a given kinetic energy exit the flux tube, other electrons of the same kinetic energy will enter the flux tube maintaining a distribution function within that flux tube. Rather than considering the electron content of a dayside magnetic flux tube, one could think of the simulations as following the evolution of the electron content of an entire dayside flux surface.

Simulations are run, typically, for a 24-hr-long interval driven by a time series of spacecraft measurements of the magnetic-field strength in the dayside magnetosphere at geosynchronous orbit (Figure 1, which is described in section 3.2). Electrons of different kinetic energies orbit the Earth at different speeds, but each energetic electron spends approximately the same fraction of a day in the dayside magnetosphere. Since azimuthal angular drift speeds tend to be higher on the nightside than on the dayside [cf. sect. (1.6) and sect (3.3) of *Roederer and Zhang*, 2014], electrons spend more than half a day in the dayside magnetosphere during 1 day of elapsed time.

The global magnetic-field-strength changes in the dayside magnetosphere are associated with changes in the intensity and the radial location of the Chapman-Ferraro current on the dayside magnetopause. Electron guiding centers move with magnetic-flux surfaces in the induction electric fields associated with temporal changes in the magnetic-field strength $\partial\vec{B}/\partial t$ so that (1) the electron experiences a change in the field strength $\Delta B = \int (dB/dt)dt$ and (2) μ is conserved for the electron, as long as the timescale of the field change is longer than the electron gyroperiod [*Borovsky and Hansen*, 1990, 1991]. These two things are true regardless of the electron's kinetic energy. Electrons with kinetic energies of 1 MeV or more cross the dayside magnetosphere in about 2 - 5 minutes or less. For dayside field compressions that are

slower than these crossing times, the relativistic electrons make one or more passes across the dayside magnetosphere during a single slow compression and make one or more passes across the dayside magnetosphere during a single slow decompression. Each time the electron passes through the dayside, it experiences a change in the field strength that is roughly $\tau_{\rm cross}\, dB/dt$ where $\tau_{\rm cross}$ is the dayside crossing time and dB/dt is the rate of field change on the electron's flux surface. While the electron is crossing the nightside magnetosphere, it may not be experiencing a change in the magnetic-field strength, depending on what the inductive electric field in the nightside is. Ignoring the complexity of what may be happening in the nightside magnetosphere, for slow compressions the compression efficiency may be reduced by a factor of 2 for very energetic electrons since the electron is only in the dayside about half of the time and only experiences half of time-integrated ΔB. Hence, the magnetic-pumping efficiencies may be reduced for high-energy electrons in slow compression: this is not accounted for in the simulations. Fortunately the magnetic-field time series of Figure 1 is dominated by faster compressions, wherein the magnetic-pumping efficiency of very energetic electrons is less reduced. (Note that fast compressions are still slow compared with electron gyroperiods and electron bounce periods.)

A further approximation made in this very basic assessment of magnetic pumping is that radial diffusion associated with the combined action of pitch-angle scattering and shell splitting [e.g. *Falthammar and Walt*, 1969; *Roederer and Schulz*, 1969; *Borovsky et al.*, 2014] is ignored: pitch-angle scattering is accounted for but shell splitting is ignored.

3.1. The Magnetic-Pumping Simulation Code

To examine the contribution of compressional magnetic pumping to the evolution of the outer electron radiation belt during high-speed-stream-driven storms, numerical simulations of the magnetic pumping of the electron-radiation-belt population are performed using the magnetic-pumping simulation code described in the Appendix of *Borovsky et al.* [1981]. The evolution of electron distribution functions under the action of the compressional

magnetic-pumping process is simulated by advecting and diffusing elements of the distribution function on a two-dimensional grid in momentum versus pitch-angle space [cf. *Borovsky et al.*, 1981; *Borovsky*, 1986]. The simulation grid is shown in Figure 2, with coordinates $p = \gamma m_e v$ (horizontal) and equatorial pitch angle α (vertical). The simulations operate on the quantity

$$n(p,\alpha) \quad = \quad 2\ v\ \tau_b\ \sin\alpha\ \cos\alpha\ f(p,\alpha) \quad , \tag{1}$$

where $n(p,\alpha)dpd\alpha$ is the number of electrons in a flux tube with momentum p and equatorial pitch-angle α, where $f(p,\alpha)$ is the phase-space distribution of the electrons (assumed to be gyrotropic), where v is the velocity of an electron with momentum p, and where $\tau_b(\alpha)$ is the pitch-angle dependent portion of the electron bounce time in a dipole magnetic field, approximated as $\tau_b(\alpha) \approx 1.30$ - $0.56\ \sin\alpha$ in units of seconds [*Hamelin et al.*, 1961; *Lyons et al.*, 1972]. In the sketch of Figure 2 the coordinates of a typical simulation are shown with α going from 0° to 90° and with momentum p going from 0 to 21 $m_e c$. The kinetic energies of electrons $E = (\gamma - 1)m_e c^2$ are denoted with the red arrows in Figure 2. The green shading on the grid denotes the extent of the atmospheric loss cone. (Note that the deviation of the loss cone away from the equatorial pitch angle $\alpha = 0°$ [cf. *Porazik et al.* 2014], which becomes important at geosynchronous orbit for electrons with energy of about 10 MeV and higher, is not accounted for in the simulations.) A typical simulation uses a grid that is 2401 gridspaces in p and 91 gridspaces in α.

To account for the evolution of the electron distribution function under the action of compression and decompression, the elements of the distribution $n(p,\alpha)$ are advected in $p-\alpha$ space conserving the first and second adiabatic invariants μ and J for motion in a dipolar magnetic field as the magnetic-field strength changes [*Goertz*, 1978; *Borovsky et al.*, 1981]. When the magnetic-field strength B increases, conservation of $\mu = p_\perp^2/B$ causes the elements of $n(p,\alpha)$ to advect to higher values of p and to larger values of α; a decrease of the magnetic-field strength leads to advection to lower values of p and smaller values of α. A conservative advection scheme is used that moves

the values of the distribution $n(p,\alpha)$ on the gridpoints forward in time and then linearly interpolates those values onto an updated $p-\alpha$ grid. As will be quantified in section 4.1, this advection scheme introduces a numerical diffusion into the simulations.

Pitch-angle scattering is implemented by numerically solving the bounce-averaged pitch-angle-diffusion equation (cf. eq. (10) of *Lyons et al.* [1972])

$$\frac{\partial f}{\partial t} \;=\; \frac{1}{\tau_b(\alpha)\,\sin\!\alpha\,\cos\!\alpha}\;\frac{\partial}{\partial\alpha}\left[\tau_b(\alpha)\,\sin\!\alpha\,\cos\!\alpha\;D_{\alpha\alpha}\;\frac{\partial f}{\partial\alpha}\right] \qquad (2)$$

with energy-dependent pitch-angle diffusion coefficients $D_{\alpha\alpha}(p,\alpha)$ calculated for the observed spectra of chorus waves and EMIC waves near geosynchronous orbit (cf. section 3.3). Using expression (1) and defining

$$H(p,\alpha) \;=\; -\,D_{\alpha\alpha}(p,\alpha)\;\frac{\partial}{\partial\alpha}\left[\log\left(\tau_b\,\sin\!\alpha\,\cos\!\alpha\right)\right] \quad , \qquad (3)$$

(where $\tau_b = 1.30\;-\;0.56\,\sin\!\alpha$ is a function of α), expression (2) becomes

$$\frac{\partial n}{\partial t} \;=\; \frac{\partial}{\partial\alpha}\left[D_{\alpha\alpha}\;\frac{\partial n}{\partial\alpha}\right] \;+\; \frac{\partial}{\partial\alpha}\left[Hn\right] \quad , \qquad (4)$$

where n, H, and $D_{\alpha\alpha}$ are all functions of p and α. In the simulations expression (4) is implicitly solved with an iterative tridiagonal algorithm as outlined in Appendix 1 of *Borovsky et al.* [1981].

In the computer simulations the two processes (magnetic compression and pitch-angle scattering) are temporally interleaved with a small change in the field strength B implemented, then the pitch-angle scattering for the small time increment is implemented, and the compression-scattering cycle is repeated. A timestep of 1 minute is used for the change in the magnetic-field strength, followed by 1-min of pitch-angle scattering. This 1-min timestep is shorter than the timescale for strong diffusion.

3.2. Magnetic-Field Compressions $\Delta B/B$ of the Dayside Magnetosphere

Temporal compression of the dayside magnetic field of the Earth was analyzed by *Borovsky and Denton* [2016]. Measurements of the magnetic-field

strength $B(t)$ at geosynchronous orbit in the dayside magnetosphere were examined and compared with a mathematical model of the compression of the dayside magnetic field by temporal variations in the solar wind. The radial motions of flux surfaces in the dayside magnetosphere were followed in the compression model. Because electrons move radially with flux surfaces, it was concluded in *Borovsky and Denton* [2016] that the particles in the dayside magnetosphere experience a magnetic-field temporal compression that is about twice as large as the magnetic-field strength change measured by a spacecraft.

The quantity$\Delta B/B$ (where B is the magnetic-field strength $|\vec{B}|$) is the quantity that is relevant for the description of plasma compressions and decompressions. For the simulations, measurements of the magnetic-field strength $B(t)$ in the dayside magnetosphere from the GOES spacecraft are used. For the GOES spacecraft in geosynchronous orbit, long continuous data intervals from the dayside magnetosphere are not obtained, so multiple intervals from multiple dayside passes are strung together in time to produce a longer continuous interval of $B(t)$. In Figure 1 one such long interval is plotted. To determine the time variation of B and to remove the systematic local-time variation in the baseline of the magnetic-field strength, the quantity $\Delta B = B(t)$ - $\langle B(t)\rangle_{90}$ is determined from the GOES measurements where $\langle B(t)\rangle_{90}$ is the 90-minute running average of $B(t)$. In Figure 1 $\Delta B = B(t)$ - $\langle B(t)\rangle_{90}$ is plotted with 1-min time resolution for 1 day of time, constructed from 7 passes of GOES 10 and GOES 12 across the dayside magnetosphere (from 10 - 14 LT) during the first day of several high-speed-stream-driven storms in the year 2003. Each separate spacecraft pass is plotted in a different color and the data from one pass to the next is connected via a linear interpolation over a 5-min period. To get $\Delta B/B$ for the magnetic-pumping simulations, the measured quantity $\Delta B = B(t)$ - $\langle B(t)\rangle_{90}$ is multiplied by 2 to account for the fact that particles in the dayside magnetosphere experience approximately twice the magnetic compression as measured by a stationary spacecraft [*Borovsky and Denton*, 2016]. This $2\Delta B$ is then is divided by B_o = 110 nT, a typical magnetic-field strength in the dayside magnetosphere at

geosynchronous orbit.

3.3. Pitch-Angle Diffusion Coefficients $D_{\alpha\alpha}$

To simulate the pitch-angle scattering of electrons by whistler-mode chorus waves, the bounce-averaged pitch-angle-diffusion coefficients $D_{\alpha\alpha}(p,\alpha)$ calculated for whistler-mode chorus waves by *Horne et al.* [2013] are algebraically parameterized. Those $D_{\alpha\alpha}$ coefficients are plotted as the solid curves in the top panel of Figure 3, and the algebraic $D_{\alpha\alpha}$ parameterizations are plotted as the dashed curves in the top panel of Figure 3. The $D_{\alpha\alpha}(p,\alpha)$ coefficients are for a combination of upper-band and lower-band chorus emission in the 9 - 12 LT sector at $L^* = 6.5$ and Kp > 4. The algebraic parameterization of the pitch-angle-diffusion coefficients $D_{\alpha\alpha}(p,\alpha)$ is give by

$$D_{\alpha\alpha} = 10^{-Q} \tag{5a}$$

$$Q = C_0 + \frac{\alpha}{30^\circ}\,(C_{30} - C_0) \qquad \text{for } \alpha \le 30^\circ \tag{5b}$$

$$Q = C_{30} + \frac{\alpha - 30^\circ}{60^\circ}\,(C_{90} - C_{30}) \qquad \text{for } \alpha \ge 30^\circ \tag{5c}$$

$$C_0 = 2.787 + 0.333\,\log_{10}(E) \qquad \text{for } E \le 251 \text{ keV} \tag{5d}$$

$$C_0 = -11.7 + 6.42\,\log_{10}(E) \qquad \text{for } E \ge 251 \text{ keV} \tag{5e}$$

$$C_{30} = 3.196 + 0.746\,(\log_{10}(E) - 1.524)^2 \tag{5f}$$

$$C_{90} = 10.07 - 3.897\,\log_{10}(E) \qquad \text{for } E \le 56 \text{ keV} \tag{5g}$$

$$C_{90} = 3.02 + 0.16\,\log_{10}(E) \qquad \text{for 56 keV} \le E \le 1 \text{ MeV} \tag{5h}$$

$$C_{90} = -4.0 + 2.5\,\log_{10}(E) \qquad \text{for } E \ge 1 \text{ MeV} \tag{5i}$$

where $D_{\alpha\alpha}(p,\alpha)$ is in units of radian^2/s, where E is the electron energy in units of keV, and where α is the equatorial pitch angle of the electron in degrees.

To simulate the pitch-angle scattering of electrons by electromagnetic ion-cyclotron waves (EMIC) in the plasmaspheric drainage plume of the dayside magnetosphere [c.f. *Borovsky et al.*, 2014] (or in the dayside magnetosphere

in general), the bounce-averaged pitch-angle-diffusion coefficients $D_{\alpha\alpha}(p,\alpha)$ calculated for EMIC waves by *Ukhorskiy et al.* [2010] are algebraically parameterized for use in the magnetic-pumping code. Using Fig. 3c of *Ukhorskiy et al.* [2010], the following parameterization is used:

$$D_{\alpha\alpha} = D_o \qquad \text{for } \alpha \leq \alpha_1 \tag{6a}$$

$$D_{\alpha\alpha} = D_o \frac{(\alpha_2 - \alpha)}{10^\circ} \qquad \text{for } \alpha_1 \leq \alpha \leq \alpha_2 \tag{6b}$$

$$D_{\alpha\alpha} = 0 \qquad \text{for } \alpha \geq \alpha_2 \tag{6c}$$

$$\alpha_2 = 85^\circ \frac{E^*}{E^* + 23.4} + \frac{E}{1360} \qquad \text{for } E \geq 400 \text{ keV} \tag{6d}$$

$$\alpha_2 = 0^\circ \qquad \text{for } E < 400 \text{ keV} \tag{6e}$$

$$\alpha_1 = \alpha_2 - 10^\circ \tag{6f}$$

$$E^* = (E - 400)^{0.622} \tag{6g}$$

where $D_{\alpha\alpha}(p,\alpha)$ is in units of radian^2/s, where E is the electron energy in units of keV, and where α is the equatorial pitch angle of the electron in degrees. The parameterized values of $D_{\alpha\alpha}(p,\alpha)$ are plotted as the solid curves in the bottom panel of Figure 3 for the value $D_o = 5.8\times10^{-3}$ radians^2 s^{-1}. For most simulations the value $D_o = 500$ radians^2 day^{-1} $= 5.8\times10^{-3}$ radians^2 s^{-1} [cf. *Albert*, 2008; *Ukhorskiy et al.*, 2010] is used.

4. Simulation Results

To study the energization of the outer electron radiation belt by compressional magnetic pumping, simulations are run in two manners: as initial-value problems and as boundary-value problems. Initial-value-problem simulations (Section 4.1) start out with an initial energy distribution of electrons and evolve that distribution in time without the presence of a continuously maintained population of seed electrons. Boundary-value-problem simulations (Section 4.2) specifically maintain a population of low-energy electrons (maintaining a boundary condition on the low-energy portion of the distribution function) and track in time the evolution of higher-energy electrons from this seed population.

For all cases, the magnetic-field-strength temporal profile used in the simulations is the composite created from measurements by GOES 10 and GOES 12 in the dayside magnetosphere in geosynchronous orbit (Figure 1), as described in section 3.2. The magnetic-field strength changes once per minute for 1 day (1440 minutes). The pitch-angle scattering in the simulations is implemented from either the upper- and lower-band chorus-wave diffusion coefficients or from the dayside EMIC-wave pitch-angle diffusion coefficients, as described in section 3.3. In all cases the atmospheric loss cone is active in the simulations.

4.1. Initial-Value-Problem Simulations

In the initial-value-problem simulations, the evolution of an initial energy distribution of electrons is followed in time. The initial distributions are isotropic in pitch angle. A narrow energy slice is used in each simulation in order to determine the action of magnetic pumping on the various energy ranges in the outer electron radiation belt and in the population of lower-energy seed electrons.

In Figure 4 the evolution of six narrow energy slices are shown after 24 hours of chorus-catalyzed compressional magnetic pumping from six separate simulations. In Figure 4 the pitch-angle scattering of the electrons is by whistler-mode chorus waves. These six simulations are plotted in six different

colors. For the six simulations the initial ($t = 0$) energy distributions are plotted as the dashed curves and the final ($t = 1$ day) distributions are plotted as the solid curves. The plotted distributions are integrated over all pitch angles. Note in Figure 4 that all six cases show a significant spread in energies after 1 day of magnetic pumping with production of electron energies that are much higher than the initial energies. Note that there is also spreading of the electron distributions to lower energies. Because the chorus-wave pitch-angle scattering is faster at lower energies (i.e. $D_{\alpha\alpha}$ is larger at lower energies as shown in Figure 3), the magnetic-pumping process is more efficient at lower energies. This results in a larger spread in energies for electrons starting out at lower energies: for example the 50-keV initial distribution (green) in Figure 4 evolves to energies of several times 50 keV whereas the 2-MeV initial energy distribution (purple) evolves to only about twice 2 MeV.

In Figure 5 the evolution of four electron energy slices are plotted after one day of EMIC-catalyzed compressional magnetic pumping with EMIC waves producing the pitch-angle scattering. The four simulations are plotted in four different colors; all plotted curves are integrals of all pitch angles. Again, the dashed curves are the initial ($t = 0$) energy distributions and the solid curves are the final ($t = 1$ day) energy distributions. At energies below 400 keV the EMIC pitch-angle-diffusion coefficients $D_{\alpha\alpha}$ are zero, so magnetic pumping should not act on electrons with energies below 400 keV when EMIC provides the scattering. The spread in the 200-keV distribution (light blue curve in Figure 5) at $t = 1$ day is produced by numerical diffusion in the advection scheme of the magnetic-pumping simulation code. The numerical diffusion in momentum (energy) works as follows. When the magnetic-field strength changes, each element of the electron distribution function that is exactly on each p-α grid point is advected to a new location in p and α (conserving 2 adiabatic invariants). That new location is not exactly on a grid point, so the electron distribution advected to the new location is linearly interpolated onto the four nearest grid points. What was a delta function in density is spread in the p direction and in the α direction. In the p direction the average

distance of spreading is 0.5 δp each time the distribution is advected, where δp is the numerical grid spacing in the p direction. Repeated advections result in repeated spreading. A numerical diffusion coefficient in the p direction can be constructed: $D_{\text{numerical}} = (0.5\ \delta p)^2/\delta t$, where δt is the advection timestep. Using $\partial f/\partial t = D_{\text{numerical}}\ \partial^2 f/\partial p^2$, the spread Δp in the momentum direction in a time t = 1 day = 1440 δt advection steps can be approximated by Δp $= (D_{\text{numerical}} t)^{1/2} = [(0.5\ \delta p)^2\ 1440] = 19\ \delta p$. Hence in a 24-hour simulation numerical diffusion will spread an initial shape by about 19 gridspaces in each direction, increasing a narrow slice to about 38 grid spaces. That is the amount of momentum spreading seen in the blue curve of Figure 5. In the magnetic-pumping simulations, numerical diffusion is controlled by using a grid with small gridspaces δp in the momentum p direction; this requires a lot of gridpoints in the p direction on the numerical mesh. (Typically 2401 gridspaces in p are used, and on occasion 3601 gridspaces.) The other 1-day curves in Figure 5 have unusual shapes, with two components, which are explained as follows. In the simulations the initial energy slices are taken to be isotropic in equatorial pitch angle; hence there are initial electrons with all pitch angles from $\alpha = 0^\circ$ to $\alpha = 90^\circ$. For EMIC waves, the pitch-angle-diffusion coefficients $D_{\alpha\alpha}(\alpha)$ are zero near $\alpha = 90^\circ$ (cf. bottom panel of Figure 3). This is particularly true for E = 500-keV electrons where (cf. expressions (6c) and (6d)) $D_{\alpha\alpha}(\alpha) = 0$ for $36.8^\circ \leq \alpha \leq 90^\circ$. The initial electrons in the $36.8^\circ \leq \alpha \leq 90^\circ$ range will not take part in the magnetic pumping process, but they will numerically diffuse as they are advected on the p-α grid as the magnetic field changes with time. For the two-component distributions of Figure 5, the narrow component is comprised of the initial electrons that are not being pumped. The broad component is comprised of the initial electrons that are caught up in the magnetic pumping process.

Examining Figures 4 and 5, two general conclusions about the production of energetic tails on the energy distributions are (1) that chorus-catalyzed magnetic pumping is more efficient at lower energies than it is at high energies and (2) that EMIC-catalyzed magnetic pumping is more effective at higher energies than it is at lower energies. Further (depending of course on the

amplitudes of the chorus and the EMIC), EMIC tends to be more effective than chorus at enabling the magnetic pumping of high-energy radiation belt electrons.

For the initial-value-problem simulations of Figures 4 and 5, the 1-day change in the average energy of the electron distribution is plotted as a function of the initial energy of the electrons in Figure 6. The vertical axis is the mean energy of the electrons $\langle E \rangle$ after 1 day of pumping divided by the initial energy of the electrons E_o. This is akin to a "heating rate" for the population. In Figure 6 the blue curve is for chorus-catalyzed magnetic pumping and the green curve is for EMIC-catalyzed magnetic pumping. Note that there are loss-cone losses of electrons in the simulations and that these mean energies $\langle E \rangle$ are the mean energies of the electrons that survive. The chorus-catalyzed magnetic pumping (blue) shows a much stronger fractional heating rate for what might be considered the seed population of electrons for the radiation belt, energies of 50 - 200 keV. According to Figure 6 the mean energy of those electrons increases by 30% - 40% after 1 day of magnetic pumping. For example, a 1-day heating rate of 32% for 200-keV electrons in Figure 6 corresponds to an average energy increase of 62-keV per day per electron. Much of this increase of the mean energy is owed to the stronger loss-cone losses at lower energies leaving predominantly higher energies. In Figure 6, for higher initial energies the rate of heating is more modest, about 5% - 10% after 1 day of chorus-catalyzed magnetic pumping. The heating rates for EMIC-catalyzed magnetic pumping (green curve) are also modest, about 0% to 10% after 1 day. Note that the value of $\langle E \rangle / E_o$ for EMIC is in part dependent on the fraction of the initial electrons that do not take part in the magnetic-pumping process because their initial pitch angles are too great, which is significant for $E_o = 500$ keV.

In Figure 7 the loss of electrons into the loss cone is examined for the initial-value-problem simulations of Figures 4 and 5. Here the ratio of the integral $\int \int n(p, \alpha) d\alpha dp$ of the energy distribution function N at time t to the integral of the initial energy distribution function N_o at time $t = 0$ is plotted as a function of time in the simulations. For lower-energy electrons

subject to pitch-angle scattering by chorus waves the loss of electrons from the simulation is substantial. At higher energies for scattering by chorus the loss rates into the atmosphere are small. As can be seen in Figure 3 $D_{\alpha\alpha}(\alpha)$ is small near $\alpha = 0°$ at higher energies, so electron pitch-angle scattering into the loss cone is slow. For EMIC waves the pitch-angle-diffusion coefficient $D_{\alpha\alpha}(\alpha)$ is robust near $\alpha = 0°$ so electrons flow strongly into the atmospheric loss cone in the EMIC-catalyzed simulations. Note in Figure 7 that the loss rate of 500-keV electrons under EMIC (red dashed curve) is not as strong as the loss rates of 1-MeV and 2-MeV initial electrons under EMIC (blue dashed and purple dashed curves); this is because a substantial portion of the initial 500-keV electrons are not subject to pitch-angle scattering since $D_{\alpha\alpha}(\alpha) = 0$ for EMIC for $\alpha \geq 36.8°$ at 500 keV and those electrons are not lost (neither are they energized by magnetic pumping: see the narrow distributions in Figure 5).

4.2. Boundary-Value-Problem Simulations

The magnetic-pumping simulations are run in a boundary-value fashion to examine the production of energetic electrons from a constant (in time) population of lower-energy seed electrons. The idea is that the seed electrons [cf. *McDiarmid and Burrows*, 1965; *Friedel et al.*, 2002; *Borovsky*, 2017] are constantly injected into the dipolar magnetosphere by substorms that occur throughout the duration of a high-speed-stream-driven storm. At geosynchronous orbit, substorm injected electrons have typical kinetic energies of 50 - to 300 keV [*Lezniak et al.*, 1968; *Cayton et al.*, 1989; *Birn et al.*, 1998, 2000; *Denton et al.*, 2010], although under special circumstances electrons with energies of 1 MeV can be injected by substorms [cf. *Ingraham et al.*, 2001; *Borovsky et al.*, 2016].

Figure 8 shows the results of three simulations: (1) when a population of electrons is maintained at $E \leq 50$ keV (green curve), (2) when a population of electrons is maintained at $E \leq 100$ keV (orange curve), and (3) when a population of electrons is maintained at $E \leq 200$ keV (blue curves). The energy distribution functions (integrated over all pitch angles) in the three

simulations are shown after 24 hours of chorus-catalyzed magnetic pumping (solid curves) and also after 1 hr and 6 hr for the 200-keV seed population (dashed blue curves). As can be seen, the magnetic-pumping process catalyzed by chorus waves can produce energetic electrons from the low-energy seed population with kinetic energies of an order of magnitude larger than the seed-population energies. The blue curves of Figure 8 show the temporal growth of the high-energy tail as the tail becomes more robust with time.

Note that since the pitch-angle-diffusion coefficient $D_{\alpha\alpha}$ for EMIC waves is zero for energies less than 400 keV, the EMIC-catalyzed magnetic-pumping process cannot energize seed electrons into high-energy radiation-belt electrons.

5. Comparison with Chorus-Wave Energy Diffusion

For a comparison of the action of compressional magnetic pumping with direct energy diffusion by chorus waves, the results of magnetic-pumping simulations are compared with the results of momentum-diffusion calculations for chorus waves. On a two dimensional grid (as in Figure 2) in p-versus-α the momentum-diffusion equation

$$\frac{\partial\, f}{\partial\, t} \;=\; \frac{1}{p^2}\,\frac{\partial}{\partial p}\,\left[p^2\; D_{pp}\;\frac{\partial f}{\partial p}\right] \tag{7}$$

is numerically solved using the energy-diffusion coefficients D_{EE} of *Horne et al.* [2013] and the pitch-angle diffusion equation (expression (2)) is numerically solved using the pitch-angle diffusion coefficients $D_{\alpha\alpha}$ of *Horne et al.* [2013]. The same chorus-wave conditions are used as in the magnetic-pumping calculations: upper- and lower-band chorus for Kp > 4 at L^*=6.5 in the 9-12 LT sector. The $D_{EE}(E,\alpha)$ coefficients of *Horne et al.* [2013] are plotted in Figure 9a in units of keV^2 s^{-1}. Using eq (29) of *Glauert and Horne* [2005]

$$D_{pp} \;=\; \frac{1}{c^2}\;\frac{(E\;+\;E_o)^2}{E\;(E\;+\;2E_o)}\;D_{EE} \tag{8}$$

the momentum-diffusion coefficients D_{pp} are obtained from D_{EE}. In Figure 9b the momentum-diffusion coefficients $D_{pp}(E,\alpha)$ are plotted in units of (gm cm/s)^2 s^{-1}. It is seen that $D_{pp}(\alpha)$ has a flat region, with $D_{pp}(\alpha)$ declining in magnitude near $\alpha = 90^\circ$ for low energies and $D_{pp}(\alpha)$ declining in magnitude near $\alpha = 0^\circ$ for high energies. In the momentum diffusion simultions, that region $20^\circ < \alpha < 80^\circ$ is fit by a constant value:

$$D_{pp} \;=\; 7.1\times 10^{-39} \qquad \text{for } E \;>\; 200 \text{ keV} \tag{9a}$$

$$D_{pp} \;=\; 1.4\times 10^{-39} \;+\; \frac{(E-60)}{140}\,5.7\times 10^{-39} \qquad \text{for } 200\text{keV} \;<\; E \;<\; 60 \text{ keV} \tag{9b}$$

$$D_{pp} \;=\; 1.4\times 10^{-39} \qquad \text{for } E \;<\; 60 \text{ keV} \quad , \tag{9c}$$

where D_{pp} has units of (gm cm/s) s^{-1} and where the electron energy E is in keV. The $D_{pp}(E)$ values of expression (9) will be taken to be independent

of the pitch-angle α. Along with this approximation, the coefficients $D_{p\alpha}$ and $D_{\alpha p}$ are ignored. Using expressions (9) for D_{pp}, the momentum-diffusion equation of expression (7) is computationally solved using the methodology of *Borovsky and Eilek* [1986]. The quantity $n(p) \equiv 4\pi p^2\ f(p)$ is defined, and with this definition expression (7) becomes the parabolic equation

$$\frac{\partial n}{\partial t} \ = \ \frac{\partial}{\partial p}\ \left[D_{pp}\ \frac{\partial n}{\partial p}\ +\ H\ n \right] \qquad , \tag{10}$$

where $H \equiv$ -$2D_{pp}/p$ and $D_{pp} = D_{pp}(p)$. Expression (10) is solved on the $\alpha =$ constant rows of the $p - \alpha$ grid with the numerical scheme of *Borovsky and Eilek* [1986], which includes a truncation-interpolation scheme at the high-momentum boundary to reduce boundary effects in the parabolic differential equation. In a single 1-minute time step, the momentum-diffusion equation (expression (10)) is solved on the $\alpha =$ constant rows of the grid for 1-minute worth of momentum diffusion and then the pitch-angle-diffusion equation (expression (4)) is solved on the $p =$ constant columns of the grid for 1-minute worth of pitch-angle diffusion. This 1-minute time step is repeated 1440 times to estimate the evolution of an initial distribution of electrons after 1 day under the action of chorus-wave energy diffusion and chorus wave pitch-angle scattering into the loss cone.

In Figure 10 the initial-value-problem evolution of energy-slice distribution functions (black dashed curves) under the action of 1 day of chorus-wave momentum diffusion are plotted in red. The initial slice energies are 100 keV in the top panel, 500 keV in the middle panel, and 1 MeV in the bottom panel. For comparison the evolution of the black initial-energy slices after 1 day of chorus-catalyzed magnetic pumping are plotted in blue and the evolution after 1 day of EMIC-catalyzed magnetic pumping are plotted in green. Note that EMIC-catalyzed magnetic pumping does not act on electrons with energies less than 400 keV. Comparing the red and blue curves in Figure 10, the energy diffusion (red) by chorus waves clearly produces a more-robust population of energetic electrons than does chorus-catalyzed magnetic pumping (blue) for all of the energy slices shown. Comparing the red and green curves in the middle panel of Figure 10, for initial electron energies of 500

keV chorus-wave energy diffusion (red) produces a more-robust population of energetic electrons than does EMIC-catalyzed magnetic pumping (green). For initial energies of 1 MeV (bottom panel of Figure 10) EMIC-catalyzed magnetic pumping and chorus-wave energy diffusion both produce strong energetic-electron populations.

In Figure 11 magnetic pumping is again compared with energy diffusion by chorus waves, this time by examining the phase-space density of electrons at fixed energies. In each of the three panels of Figure 11 an initial isotropic distribution of electrons with a narrow range of energies is used as input to initial-value-problem simulations, and the phase-space density at a higher kinetic energy is examined. In Figure 11a the initial energies are from 242 keV to 260 keV, in Figure 11b the initial energies are from 493 keV to 517 keV, and in Figure 11b the initial energies are from 986 keV to 1013 keV. In the simulations of Figure 11 the loss cone operates at all times. Figure 11a examines the energization from 250 keV to 500 keV: plotted in blue is the pitch-angle-averaged phase-space density at 500 keV in the chorus-catalyzed magnetic-pumping simulation and in red the pitch-angle-averaged phase-space density at 500 keV in the chorus-wave energy diffusion simulation. The blue curve in Figure 11a is irregular because the phase-space density at fixed energy varies in time as the magnetic field is compressed and decompressed. Note the rapidity of the energization from 250 keV to 500 keV in the energy diffusion simulation. Figure 11b examines the energization from 500 keV to 1 MeV: the blue curve is for chorus-catalyzed magnetic pumping, the green curve is for EMIC-catalyzed magnetic pumping, and the red curve is for chorus-wave energy diffusion. Note again the rapidity of the energization in the energy-diffusion simulation. In Figure 11b the chorus-catalyzed and the EMIC-catalyzed magnetic pumping are similar in their abilities to energize electrons from 500 keV to 1 MeV. (Dependent on the amplitude of chorus and EMIC waves.) Figure 11c examines the energization from 1 MeV to 2 MeV: the blue curve is for chorus-catalyzed pumping, the green curve is for EMIC-catalyzed pumping, and the red curve is for chorus-wave energy diffusion. Again the chorus-wave energy diffusion (red) provides the

most-rapid energization, followed by the EMIC-catalyzed magnetic pumping (green). Figure 11 verifies the finding that compressional magnetic pumping is not as powerful as chorus-wave energy diffusion for energizing electrons.

For the parameters used in these simulations, compressional magnetic pumping in the dayside magnetosphere at geosynchronous orbit during high-speed-stream-driven storms is not as strong a producer of energetic electrons as is chorus-wave energy diffusion.

6. Discussion

Compressional magnetic pumping does not appear to be a dominant mechanism for energizing the outer electron radiation belt during high-speed-stream-driven storms. In Section 5 it was found that chorus-wave energy diffusion produces a much-more-robust energetic-electron population from lower-energy electrons. For the production of a high-energy tail on the electron energy distribution, EMIC-catalyzed magnetic pumping is more efficient than is chorus-catalyzed magnetic pumping. Since EMIC waves are much less efficient at directly accelerating electrons than are chorus waves [cf. *Horne and Thorne*, 1998; *Glauert and Horne*, 2005], it is possible that compressional magnetic pumping could be a dominant energization mechanism in the dayside magnetosphere if EMIC waves are present and chorus waves are not. In some locations this is possible: near geosynchronous orbit EMIC is mainly observed at local noon and in the afternoon [e.g. *Bossen et al.*, 1976; *Anderson et al.*, 1992] while chorus amplitudes are weak in the afternoon sector [e.g. *Horne et al.*, 2005a; 2013]. The efficiency of EMIC-catalyzed magnetic pumping for producing energetic electrons is somewhat insensitive to the EMIC-wave amplitudes over a large range of amplitudes as shown in Figure 12 where a 2-MeV initial distribution of electrons is subjected to 1-day of compressional magnetic pumping catalyzed by EMIC waves with different amplitudes as gauged by the value of D_o in expressions (6).

With strong enough $\Delta B/B$ compressions by the solar wind, compressional magnetic pumping could be the dominant energization mechanism in the dayside magnetosphere. At geosynchronous orbit during typical high-speed-stream-driven storms this is not likely to be the case, but during sheath driven storms it might be. In the top panel of Figure 13 the superposed epoch average of the 10-minute change in the solar-wind ram pressure ΔP_{ram10} (as measured by the SWEPAM instrument [*McComas et al.*, 1998] on ACE) is plotted in blue for 70 high-speed-stream-driven storms and in red for 47 coronal-mass-ejection (CME) sheaths. The zero epoch for the blue curve is the onset of the high-speed-stream-driven storm, which occurs while a corotating interaction region (CIR) is passing the Earth; the zero epoch for the

red curve is the passage of an interplanetary shock, which forms the leading edge of a CME sheath. The top panel of Figure 13 demonstrates that the temporal variations of the solar-wind ram pressure are much greater on average in CME sheaths than they are in CIRs. In the bottom panel of Figure 13 the superposed average of the 10-minute change $\Delta B_{10}/B$ in the magnetic-field strength at geosynchronous orbit in the dayside magnetosphere is plotted as measured by the fluxgate magnetometer [*Dunham et al.*, 1996] on the GOES spacecraft. Again, the zero epoch for the blue curve is the onset of the high-speed-stream-driven storm and the zero epoch for the red curve is the passage of an interplanetary shock. As seen in the bottom panel, on average the fractional compression of the dayside magnetic field by the solar wind is about a factor of 2 greater during CME sheaths than it is during CIRs. A factor of 2 increase in $\Delta B/B$ produces a factor of 4 increase in the speed of compressional magnetic pumping. Depending on the strength of EMIC in the dayside magnetosphere during sheath-driven storms, compressional magnetic pumping might be the dominant energization mechanism operating on the electron radiation belt.

The effectiveness of compressional magnetic pumping for the production of energietic electrons is probably limited to geosynchronous orbit (r = 6.6 R_E) and outward. The efficiency of compressional pumping goes as $(\Delta B/B_o)^2$ where ΔB is the amplitude of the magnetic compressions and B_o is the mean magnetic-field strength. The large spatial extents in the east-west and north-south directions of the Chapman-Ferraro current sheet on the dayside magnetopause that produces the ΔB in the dayside magnetosphere means that the amplitude of ΔB is not very sensitive to the radial distance from the Chapman-Ferraro current sheet. However, B_o varies approximately as r^3 in the dayside magnetosphere, where r is the distance from the Earth. Hence, $(\Delta B/B_o)^2$ is reduced very strongly going toward the Earth. Going outward from geosynchronous orbit, $(\Delta B/B_o)^2$ increases substantially, but the trapping of the radiation-belt electrons in this regions may be weak. Hence, compressional magnetic pumping may be very strong beyond geosynchronous orbit, the the radiation-belt population may be tenuous.

Compressional magnetic pumping should also act on the proton radiation belt with pitch-angle scattering occurring via proton interactions with EMIC waves [*Søraas et al.* 1999; *Shoji and Omura*, 2012] or with whistler-mode hiss [*Villalon and Burke*, 1994; *Kozyra et al.*, 1994]. Examining the proton radiation belt at geosynchronous orbit during 94 high-speed-stream-driven storms, *Borovsky et al.* [2016] found that the flux of 1-MeV protons systematically increases in the day prior to the onset of a high-speed-stream-driven storm. At such times before the storm onset, (1) the solar wind passing the Earth is often sector-reversal-region plasma which is very inhomogeneous [*Gosling et al.*, 1981; *Borrini et al.*, 1981] with strong temporal variations in the solar-wind ram pressure, and (2) the plasmapause often extends to beyond geosynchronous orbit owing the refilling of the outer plasmasphere [*Borovsky and Steinberg*, 2006; *Denton and Borovsky*, 2008]. These two factors may combine to produce strong $\Delta B/B$ in the dayside magnetosphere with whistler-mode hiss scattering of the protons.

In this report an assessment was made about the importance of compressional magnetic pumping in the dayside magnetosphere for the evolution of the outer electron radiation belt. The study was restricted to the dayside magnetosphere where the magnetic-field-strength variations ΔB that an electron experiences could be estimated. Before compressional magnetic pumping can be assessed for the electron radiation belt in the nightside magnetosphere, an estimate of the time variability of ΔB as seen by an electron in the nightside magnetosphere must be obtained. Assessing ΔB as seen by an electron in the nightside magnetosphere might require a program of research that combines global MHD simulations of the dynamic solar-wind-driven magnetosphere with spacecraft magnetic-field measurements in the nightside outer radiation belt.

7. Summary and Future

This investigation computationally explored the magnetic pumping of radiation-belt electrons associated with compressions of the dayside magnetosphere driven by temporal changes in the solar wind. Chorus-catalyzed magnetic pumping and EMIC-catalyzed magnetic pumping were separately simulated. The magnetic-pumping simulation results were compared with energy-diffusion calculations for chorus waves in the dayside magnetosphere. The parameters chosen for the simulations pertain to the early phase of high-speed-stream-driven storms.

The findings of this investigation are the following:

(1) If both pitch-angle scattering of electrons and magnetic compressions are present, the magnetic-pumping energization of electrons is unavoidable.

(2) Loss-cone losses of electrons operate during the magnetic-pumping energization process. When pitch-angle-scattering is efficient near 0° pitch angles (chorus waves acting on lower-energy (seed) electrons and EMIC waves acting on higher-energy electrons) the diffusion into the loss cone is more robust.

(3) Chorus-catalyzed magnetic pumping and EMIC-catalyzed magnetic pumping both produce an increase in the average energy of electrons. This increase is a combination of heating of the electron distribution by magnetic pumping and the stronger loss of lower-energy electrons into the loss cone.

(4) Both chorus-catalyzed and EMIC-catalyzed magnetic pumping produce energetic -electron populations from lower-energy electrons.

(5) Chorus-catalyzed magnetic pumping is more efficient at energizing medium-energy (50 keV to 200 keV) electrons than it is at energizing higher-energy (500 keV to 2 MeV) electrons.

(6) EMIC-catalyzed magnetic pumping does not operate on electrons with kinetic energies below about 400 keV.

(7) For higher-energy electrons (500 keV to 2 MeV), EMIC-catalyzed magnetic pumping produces more energetic electrons than does chorus-catalyzed magnetic pumping.

(8) The simulation results of compressional magnetic pumping were com-

pared with numerical calculations of direct energy diffusion by chorus waves. In general, compressional magnetic pumping is less efficient at energizing electrons than is chorus energy diffusion. The strength of this conclusion, however, depends on the amplitude $\Delta B/B$ of the dayside magnetic-field compressions and on the amplitudes of chorus and EMIC waves.

(9) Compressional magnetic pumping catalyzed by chrous-wave or EMIC-wave pitch-angle scattering is probably a minor contributor to the energization of the outer electron radiation belt during high-speed-stream-driven storms.

(10) Inward of geosynchronous orbit magnetic pumping will be much less effective.

Four future studies are suggested: (1) an assessment of the role of compressional magnetic pumping on the electron radiation belt during CME-sheath-driven storms, (2) an assessment of the compressional magnetic pumping of the proton radiation belt prior to the onset of high-speed-stream-driven storms, (3) a determination of the magnetic-field compressions that electrons undergo in the nightside magnetosphere, and (4) an analysis of compressional magnetic pumping in the nightside magnetosphere.

Acknowledgements: The authors thank Mick Denton, Sarah A. Glauert, Mike Hartinger, Mike Henderson, Tobias Kersten, and Geoff Reeves for help and for helpful conversations. This work was supported at the University of Michigan by the NASA Geospace SR&T program via grant NNX12AD29G; supported at the Space Science Institute by the NASA Heliophysics LWS TRT program via grants NNX14AN90G and NNX16AB75G, by the NSF GEM Program via award AGS-1502947, by the NSF Solar-Terrestrial Program via grant AGS-1261659, and by the NASA Heliophysics Guest Investigator Program via grant NNX14AC15G; and supported at British Antarctic Survey by UK Natural Environment Research Council National Capability funding. Simulation outputs are available upon request from the first author. JEB dedicates this paper to Glenn Joyce and Chris Goertz.

References

Albert, J. M., Efficient approximations of quasi-linear diffusion coefficients in the radiation belt, *J. Geophys. Res., 113*, A06208, 2008.

Albert, J. M., Quasi-linear diffusion coefficients for highly oblique whistler mode waves, *J. Geophys. Res., 122*, 5339, 2017.

Alfven, H., On the origin of cosmic radiation. II, *Phys. Rev., 77*, 375, 1950.

Alfven, H., On the origin of cosmic radiation, *Tellus, 6*, 232, 1954.

Alfven, H., Momentum spectrum of the Van Allen radiation, *Phys. Rev. Lett., 3*, 459, 1959.

Alfven, H., and C.-G. Falthammar, *Cosmical Electrodynamics*, Sect. 2.7.4, Oxford University Press, New York, 1963.

Anderson, B. J., R. E. Erlandson, and L. J. Zanetti, A statistical study of Pc 1-2 magnetic pulsations in the equatorial magnetosphere 1. Equatorial occurrence distribution, *J. Geophys. Res., 97*, 3075, 1992.

Artemyev, A. V., O V. Agapitov, D. Mourenas, V. V. Karasnoselskikh, and F. S. Mozer, Wave energy budget analysis in the Earth's radiation belts uncovers a missing energy, *Nature Comm., 6*, 7143, 2015.

Balikhin, M. A., R. J. Boynton, S. N. Walker, J. E. Borovsky, S. A. Billings, and H. L. Wei, Using the NARMAX approach to model the evolution of energetic electrons fluxes at geostationary orbit, *Geophys. Res. Lett., 38*, L18105, 2011.

Birn, J., M. F. Thomsen, J. E. Borovsky, G. D. Reeves, D. J. McComas, R. D. Belian, and M. Hesse, Substorm electron injections: Geosynchronous observations and test particle simulations, *J. Geophys. Res., 103*, 9235, 1998.

Birn, J., M. F. Thomsen, J. E. Borovsky, G. D. Reeves, and M. Hesse, Particle acceleration in the dynamic magnetotail, *Phys. Plasmas, 7*, 2149, 2000.

Borovsky, J. E., Magnetic pumping by magnetosonic waves in the presence of noncompressive electromagnetic fluctuations, *Phys. Fluids, 29*, 3245, 1986.

Borovsky, J. E., Induced Absorption of Extraordinary (Z-Mode) Waves

by Electron Pumping, *Phys. Fluids, 31*, 700, 1988.

Borovsky, J. E., Time-integral correlations of multiple variables with the relativistic-electron flux at geosynchronous orbit: The strong roles of the substorm-injected electrons and the ion plasma sheet, *J. Geophys. Res.*, doi:10.1002/2017JA024476, 2017.

Borovsky, J. E., and M. H. Denton, The differences between CME-driven storms and CIR-driven storms, *J. Geophys. Res., 111*, A07S08, 2006.

Borovsky, J. E., and M. H. Denton, The magnetic field at geosynchronous orbit during high-speed-stream-driven storms: Connections to the solar wind, the plasma sheet, and the outer electron radiation belt, *J. Geophys. Res., 115*, A08217, 2010a.

Borovsky, J. E., and M. H. Denton, On the Heating of the Outer Radiation Belt to Produce High Fluxes of Relativistic Electrons: Measured Heating Rates for High-Speed-Stream-Driven Storms, *J. Geophys. Res., 115*, A12206, 2010b.

Borovsky, J. E., and M. H. Denton, A survey of the anisotropy of the outer electron radiation belt during high-speed-stream-driven storms, *J. Geophys. Res., 116*, A05201, 2011.

Borovsky, J. E., and M. H. Denton, The differences between storms driven by helmet-streamer CIRs and storms driven by pseudostreamer CIRs, *J. Geophys. Res., 118*, 5506, 2013.

Borovsky, J. E., and M. H. Denton, Exploring the cross-correlations and autocorrelations of the ULF indices and incorporating the ULF indices into the systems science of the solar-wind-driven magnetosphere, *J. Geophys. Res., 119*, 4307, 2014.

Borovsky, J. E., and M. H. Denton, Compressional perturbations of the dayside magnetosphere during high-speed-stream-driven geomagnetic storms, *J. Geophys. Res., 121*, 4569, 2016.

Borovsky, J. E., and J. A. Eilek, A Study of the Stochastic Energization of Charged Particles with and without Synchrotron Energy Loss, *Astrophys. J., 308*, 929, 1986.

Borovsky, J. E., and P. J. Hansen, The Magnetic Pumping of Plasmas

with Sawtooth Waveforms, *Phys. Fluids B, 2*, 1114, 1990.

Borovsky, J. E., and P. J. Hansen, The Breaking of the First Adiabatic Invariants of Particles in Time-Dependent Magnetic Fields: Computer Simulations and Theory, *Phys. Rev. A, 43*, 5605, 1991.

Borovsky, J. E., and J. T. Steinberg, The "calm before the storm" in CIR/magnetosphere interactions: Occurrence statistics, solar-wind statistics, and magnetospheric preconditioning, *J. Geophys. Res., 111*, A07S10, 2006.

Borovsky, J. E., and K. Yakymenko, Substorm occurrence rates, substorm recurrence times, and solar-wind structure, *J. Geophys. Res., 122*, doi:10.1002/2016JA023625, 2017.

Borovsky, J. E., C. K. Goertz, and G. Joyce, Magnetic pumping of particles in the outer Jovian magnetosphere, *J. Geophys. Res., 86*, 3481, 1981.

Borovsky, J. E., R. H. W. Friedel, and M. H. Denton, Statistically measuring the amount of pitch-angle scattering that energetic electrons undergo as they drift across the plasmaspheric drainage plume at geosynchronous orbit, *J. Geophys. Res., 119*, 1814, 2014.

Borovsky, J. E., T. E. Cayton, M. H. Denton, R. D. Belian, R. A. Christensen, and J. C. Ingraham, The proton and electron radiation belts at geosynchronous orbit: Statistics and behavior during high-speed-stream-driven storms, *J. Geophys. Res., 121*, 5449, 2016.

Borrini, G., J. T. Gosling, S. J. Bame, W. C. Feldman, and J. M. Wilcox, Solar wind helium and hydrogen structure near the heliospheric current sheet: A signal of coronal streamers at 1 AU, *J. Geophys. Res., 86*, 4565, 1981.

Bossen, M., R. L. McPherron, and C. T. Russell, A statistical study of Pc 1 pulsations at synchronous orbit, *J. Geophys. Res., 81*, 6083, 1976.

Boynton, R. J., M. A. Balikhin, S. A. Billings, G. D. Reeves, N. Ganushkina, M. Gadalin, O. A. Amariutei, J. E. Borovsky, and S. N. Walker, The analysis of electron fluxes at geosynchronous orbit employing a NARMAX approach, *J. Geophys. Res., 118*, 1500, 2013.

Canobbio, E., Neoclassical theory of Landau damping and ion and electron transit-time magnetic pumping (TTMP) in toroidal geometry, *Nuclear Fusion, 12*, 561, 1972.

Cayton, T. E., R. D. Belian, S. P. Gary, T. A. Fritz, and D. N. Baker, Energetic electron components at geosynchronous orbit, *Geophys. Res. Lett., 16*, 147, 1989.

Chan, K.-W., and R. E. Holzer, ELF hiss associated with plasma density enhancements in the outer magnetosphere, *J. Geophys. Res., 81*, 2267, 1976.

Dai, L., J. R. Wygant, C. A. Cattell, S. Thaller, K. Derten, A. Beneman, X. Tang, R. H. Friedel, S. G. Claudpierre, and X. Tao, Evidence for injection of relativistic electrons into the Earth's outer radiation belt via intense substorm electric fields, *Geophys. Res. Lett., 41*, 1133, 2014.

Degeling, A. W., L. G. Ozeke, R. Rankin, I. R. Mann, and K. Kabin, Drift resonant generation of peaked relativistic electron distributions by Pc 5 ULF waves, *J. Geophys. Res., 113*, A02208, 2008.

Denton, M. H., and J. E. Borovsky, Superposed epoch analysis of high-speed-stream effects at geosynchronous orbit: Hot plasma, cold plasma, and the solar wind, *J. Geophys. Res., 113*, A07216, 2008.

Denton, M. H., and J. E. Borovsky, Magnetosphere response to high-speed solar wind streams: A comparison of weak and strong driving and the importance of extended periods of fast solar wind, *J. Geophys. Res., 117*, A00L05, 2012.

Denton, M. H., and J. E. Borovsky, The response of the inner magnetosphere to the trailing edges of high-speed solar-wind streams,*J. Geophys. Res., 122*, 501, 2017.

Denton, M. H., J. E. Borovsky, and T. E. Cayton, A density-temperature description of the outer electron radiation belt during geomagnetic storms, *J. Geophys. Res., 115*, A01208, 2010.

Dmitriev, A. V., M. F. Bakhareva, and Y. S. Minaeva, Electron acceleration by magnetic pumping on the tail magnetopause, *Adv. Space Res., 28*, 807, 2001.

Dunham, W. D., S. A. MacIntyre, and C. R. Upton, Design and performance of the GOES-8 high resolution magnetometer, *SPIE Proc., 2812*, 365, 1996.

Elkington, S. R., M. K. Hudson, and A. A. Chan, Acceleration of rela-

tivistic electrons via drift-resonant interaction with toroidal-mode PC-5 ULF oscillations, *Geophys. Res. Lett., 26*, 3273, 1999.

Elkington, S. R., M. K. Hudson, and A. A. Chan, Resonant acceleration and diffusion of outer zone electrons in an asymmetric geomagnetic field, *J. Geophys. Res., 108*, 1116, 2003.

Falthammar, C.-G., and M. Walt, Radial motion resulting from pitch-angle scattering of trapped electrons in the distorted geomagnetic field, *J. Geophys. Res., 74*, 4184, 1969.

Fok, M.-C., T. E. Moore, and W. N. Spjeldvik, Rapid enhancement of radiation belt electron fluxes due to substorm depolarization of the geomagnetic field, *J. Geophys. Res., 106*, 3873, 2001.

Friedel, R. H. W., G. D. Reeves, and T. Obara, Relativistic electron dynamics in the inner magnetosphere – A review, *J. Atmos. Solar Terr. Phys., 64*, 265, 2002.

Glauert, S. A., and R. B. Horne, Calculation of pitch angle and energy diffusion coefficients with the PADIE code, *J. Geophys. Res., 110*, A04206, 2005.

Goertz, C. K., Energization of particles in Jupiter's outer magnetosphere, *J. Geophys. Res., 83*, 3145, 1978.

Gosling, J. T., G. Borrini, J. R. Asbridge, S. J. Bame, W. C. Feldman, and R. T. Hansen, Coronal streamers in the solar wind at 1 AU, *J. Geophys. Res., 86*, 5438, 1981.

Hamlin, D. A., R. Karplus, R. C. Vik, and K. M. Watson, Mirror and azimuthal drift frequencies for geomagnetically trapped particles, *J. Geophys. Res., 66*, 1, 1961.

Hartinger, M. D., D. L. Turner, F. Plaschke, V. Angelopoulos, and H. Singer, The role of transient ion foreshock phenomena in driving Pc5 ULF wave activity, *J. Geophys. Res., 118*, 299, 2013.

Hayakawa, M., N. Ohmi, M. Parrot, and F. Lefeuvre, Direction finding of ELF hiss emissions in a detached plasma region of the magnetosphere, *J. Geophys. Res., 91*, 135, 1986.

Horne, R. B., and R. M. Thorne, Potential waves for relativistic electron

scattering and stochastic acceleration during magnetic storms, *Geophy. Res. Lett., 25*, 3011, 1998.

Horne, R.B., R. M. Thorne, S. A. Glauert, J. M. Albert, N. P. Meredith, and R. R. Anderson, Timescale for radiation belt electron acceleration by whistler mode chorus waves, *J. Geophys. Res., 110*, A03225, 2005a.

Horne, R. B., et al.,Wave acceleration of electrons in the Van Allen radiation belts, *Nature, 437*, 227, 2005b.

Horne, R. B., N. P. Meredith, S. A. Glauert, A. Varotsou, D. Boscher, R. M. Thorne, Y. Y. Shprits, and R. R. Anderson, Mechanisms for the acceleration of radiation belt electrons, *Recurrent Magnetic Storms*, Geophys. Monog. Series 167, pg. 151, American Geophysical Union, 2006.

Horne, R. B., T. Kersten, S. A. Glauert, N. P. Meredith, D. Boscher, A. Sicard-Piet, R. M. Thorne, and W. Li, A new diffusion matrix for whistler mode chorus waves, *J. Geophys. Res., 118*, 6302, 2013.

Ingraham, J. C., T. E. Cayton, R. D. Belian, R. A. Christensen, R. H. W. Friedel, M. M. Meier, G. D. Reeves, and M. Tuszewski, Substorm injection of relativistic electrons to geosynchronous orbit during the great magnetic storm of March 24, 1991, *J. Geophys. Res., 106*, 25759, 2001.

Jordanova, V. K., Y. S. Miyoshi, S. Zaharia, M. F. Thomsen, G. D. Reeves, D. S. Evans, C. G. Mouikis, and J. F. Fennell, Kinetic simulations of ring current evolution during the Geospace Environment Modeling challenge events, *J. Geophys. Res., 111*, A11S10, 2006.

Kepko, L., and H. E. Spence, Observations of discrete, global magnetospheric oscillations directly driven by solar wind density variations, *J. Geophys. Res., 108*, 1257, 2003.

Kim, H.-J., A. A. Chan, R. A. Wolf, and J. Birn, Can substorms produce relativistic outer belt electrons?, *J. Geophys. Res., 105*, 7721, 2000.

Koechlin, F., and A. Samain, New method of magnetic pumping for plasma heating, *Phys. Rev. Lett., 26*, 490, 1971.

Kovalevskiy, I. V., Ion-cyclotron instability in the frontal boundary layer of the geomagnetosphere produced by detached plasma clouds, *Geomag. Aeron., 20*, 338, 1980.

Kovalevskiy, I. V., Cyclotron instability during interaction of detached plasma regions with the plasma sheet during substorms, *Geomag. Aeron., 21*, 83, 1981.

Kozyra, J. U., C. E. Rasmussen, R. H. Miller, and L. R. Lyons, Interaction of ring current and radiation belt protons with ducted plasmaspheric hiss 1. Diffusion coefficients and timescales, *J. Geophys. Res., 99*, 4069, 1994.

Kozyreva, O., V. Pilipenko, M. J. Engebretson, K. Yumoto, J. Watermann, and N. Romanova, In search of a new ULF wave index: Comparison of Pc5 power with dynamics of geostationary relativistic electrons, *Planet. Space Sci., 55*, 755, 2007.

Kuijpers, J., L. Fletcher, M. Abada-Simon, K. D. Horne, M. A. Raadu, G. Ramsay, and D. Steeghs, Magnetic pumping in cataclysmic variable AE Aquarii, Astron. *Astrophys., 322*, 242, 1997.

Lezniak, T. W., R. L. Arnoldy, G. K. Parks, and J. R. Winkler, Measurements and intensity of energetic electrons at the equator at 6.6 R, *Radio Sci. 3*, 710, 1968.

Li, L. Y., J. B. Cao, J. Y. Yang, and Y. X. Dong, Joint response of geosynchronous magnetic field and relativistic electrons to external changes in solar wind dynamic pressure and interplanetary magnetic field, *J. Geophys. Res., 118*, 1472, 2013.

Liu, W. W., and G. Rostoker, Energetic ring current particles generated by recurring substorm cycles, *J. Geophys. Res., 100*, 21897, 1995.

Liu, W. W., G. Rostoker, and D. N. Baker, Internal acceleration of relativistic electrons by large-amplitude ULF pulsations, *J. Geophys. Res., 104*, 17391, 1999.

Lyons, L. R., R. M. Thorne, and C. F. Kennel, Pitch-angle diffusion of radiation belt electrons within the plasmasphere, *J. Geophys. Res., 77*, 3455, 1972.

Mathie, R. A., and I. R. Mann, A correlation between extended intervals of ULF wave power and storm-time geosynchronous relativistic electron flux enhancements, *Geophys. Res. Lett., 27*, 3261, 2000.

Mathie, R. A., I. R. Mann, On the solar wind control of Pc5 ULF pul-

sation power at mid-latitudes: Implications for MeV electron acceleration in the outer radiation belt, *J. Geophys. Res., 106*, 29783, 2001.

McComas, D. J., Blame, S. J., Barker, P., Feldman, W. C., Phillips, J. L., Riley, P., Griffee, J. W., Solar Wind Electron Proton Alpha Monitor (SWEPAM) for the Advanced Composition Explorer, *Space Sci. Rev. 86*, 563, 1998.

McDiarmid, I. B., and J. R. Burrows, On an electron source fore the outer Van Allen radiation zone, *Can. J. Phys., 43*, 1161, 1965.

Melrose, D. B., Acceleration of ultrarelativistic electrons in the Crab Nebula, *Astrophys. Space Sci., 4*, 165, 1969.

Meredith, N. P., R. B. Horne, and R. R. Anderson, Substorm dependence of chorus amplitudes: Implications for the acceleration of electrons to relativistic energies, *J. Geophys. Res., 106*, 13165, 2001

Meredith, N. P., R. B. Horne, R. H. A. Iles, R. M. Thorne, D. Heynderickx, and R. R. Anderson, Outer zone relativistic electron acceleration associated with substorm-enhanced whistler mode chorus, *J. Geophys. Res., 107*, 1144, 2002.

Meredith, N. P., R. B. Horne, M. M. Lam, M. H. Denton, J. E. Borovsky, and J. C. Green, Energetic electron precipitation during high-speed solar wind stream driven storms, *J. Geophys. Res., 116*, A05223, 2011.

Meredith, N. P., R. B. Horne, A. Sicard-Piet, D. Boscher, K. H. Yearby, W. Li, and R. M. Thorne, Global model of lower band and upper band chorus from multiple satellite observations, *J. Geophys. Res., 117*, A12209, 2012.

Min, K., J. Lee, and K. Keika, Chorus wave generation near the dawnside magnetopause due to the drift shell splitting of substorm-injected electrons, *J. Geophys. Res., 115*, A00I02, 2010.

Mourenas, D., A. V. Artemyev, Q. Ma, O. V. Agapitov, and W. Li, Fast dropouts of multi-MeV electrons due to combined effects of EMIC and whistler mode waves, *Geophys. Res. Lett., 43*, 4155, 2016.

Mu, J.-L., A new magnetic pumping accelerator of charged particles in Jupiter s magnetosphere, *Geophys. Res. Lett., 20*, 1463, 1993.

Murty, G. S., and R. K. Varma, Acceleration of cosmic radiation, *Phys.*

Rev., 112, 1789, 1958.

Ozeke, L. G., I. R. Mann, K. R. Murphy, I. J. Rae, D. K. Milling, S. R. Elkington, A. A. Chan, and H. J. Singer, ULF wave derived radiation belt radial diffusion coefficients, *J. Geophys. Res., 117*, A04222, 2012.

Panasyuk, M., The ion radiation belts: Experiments and models, in *Effects of Space Weather on Technology Infrastructure*, I. A. Daglis (ed.), pg. 65, Kluwer Academic, Netherlands, 2004.

Paulikas, G. A., and J. B. Blake, Modulation of trapped energetic electrons at 6.6 Re by the interplanetary magnetic field, *Geophys. Res. Lett., 3*, 277, 1976.

Porazik, P., J. R. Johnson, I. Kaganovich, and E. Sanchez, Modification of the loss cone for energetic particles, *Geophys. Res. Lett., 41*, 8107, 2014.

Roederer, J. G., and M. Schulz, Effect of shell splitting on radial diffusion in the magnetosphere, *J. Geophys. Res., 74*, 4117, 1969.

Roederer, J. G., and H. Zhang, *Dynamics of Magnetically Trapped Particles*, Springer, Heidelberg, 2014.

Romanova, N., and V. Pilipenko, ULF wave indices to characterize the solar wind-magnetosphere interaction and relativistic electron dynamics, *Acta Geophys., 57*, 158, 2009.

Rostoker, G., S. Skone, and D. N. Baker, On the origin of relativistic electrons in the magnetosphere associate with some geomagnetic storms, *Geophys. Res. Lett., 25*, 3701, 1998.

Safrankova, J., O. Goncharov, Z. Nemecek, L. Prech, and D. G. Sibeck, Asymmetric magnetosphere deformation driven by hot flow anomaly(ies), *Geophys. Res. Lett., 39*, L15107, 2012.

Sauvaud, J.-A., M. Walt, D. Delcourt, C. Benoist, E. Penou, Y. Chen, and C. T. Russell, Inner radiation belt particle acceleration and energy structuring by drift resonance with ULF waves during geomagnetic storms, J. Geophys. Res., 118, 1723, 2013.

Schluter, A., Der Gyro-Relaxations-Effect, *Z. Naturforsh., 12a*, 822, 1957.

Shprits, Y. Y., N. P. Meredith, and R. M. Thorne, Parameterization of radiation belt electron loss timescales due to interactions with chorus waves,

Geophys. Res. Lett., 34, L11110, 2007.

Shoji, M., and Y. Omura, Precipitation of highly energetic protons by helium branch electromagnetic ion cyclotron triggered emissions, *J. Geophys. Res., 117*, A12210, 2012.

Søraas, F., K. Aarsnes, J. A. Lundblad, and D. S. Evans, Enhanced pitch angle scattering of protons at mid-latitudes during geomagnetic storms, *Phys. Chem. Earth (C), 24*, 287, 1999.

Spasojevic, M., and S. A. Fuselier, Temporal evolution of proton precipitation associated with the plasmaspheric plume, *J. Geophys. Res., 114*, A12201, 2009.

Spitzer, L., and L. Witten, On the ionization and heating of a plasma, USAEC Report NYO-999, March 1953.

Summers, D., R. M. Thorne, and F. Xiao, Relativistic theory of wave-particle resonant diffusion with application to electron acceleration in the magnetosphere, *J. Geophys. Res., 103*, 20487, 1998.

Summers, D., B. Ni, N. P. Meredith, R. B. Horne, R. M. Thorne, M. B. Moldwin, and R. R. Anderson, Electron scattering by whistler-mode ELF hiss in plasmaspheric plumes, *J. Geophys. Res., 113*, A04219, 2008.

Tataronis, J. A., and W. Grossmann, On Alfven wave heating and transit time magnetic pumping in the guiding-centre model of a plasma, *Nuclear Fusion, 16*, 667, 1976.

Thorne, R. M., T. P. O Brien, Y. Y. Shprits, D. Summers, and R. B. Horne, Timescale for MeV electron microburst loss during geomagnetic storms, *J. Geophys. Res., 110*, A09202, 2005.

Thorne, R. M., R. B. Horne, V. K. Jordanova, J. Bortnik, and S. Glauert, Interaction of EMIC waves with thermal plasma and radiation belt particles, in *Magnetospheric ULF Waves*, K. Takahashi, P. J. Chi, R. E. Denton, and R. L. Lysak (eds.), pg. 213, American Geophysical Union, 2006.

Thorne, R. M., W. Li, B. Ni, Q. Ma, J. Bortnik, L. Chen, D. N. Baker, H. E. Spence, G. D. Reeves, M. G. Henderson, C. A. Kletzing, W. S. Kurth, G. B. Hospaodarsky, J. B. Blake, J. F. Fennell, S. G. Claudepierre, and S. G. Kanekal, Rapid local acceleration of relativistic radiation-belt electrons

by magnetospheric chorus, *Nature, 504*, 411, 2013.

Tu, W., S. R. Elkington, X. Li, W. Liu, and J. Bonnell, Quantifying radial diffusion coefficients of radiation belt electrons based on global MHD simulation and spacecraft measurements, *J. Geophys. Res., 117*, A10201, 2012.

Ukhorskiy, A. Y., Y. Y. Shprits, B. J. Anderson, K. Takahashi, and R. M. Thorne, Rapid scattering of radiation belt electrons by short-time EMIC waves, *Geophys. Res. Lett., 37*, L09101, 2010.

Viall, N. M., L. Kepko, L., and H. E. Spence, Relative occurrence rates and connection of discrete frequency oscillations in the solar wind density and dayside magnetosphere, *Geophys. Res. Lett., 114*, A01201, 2009.

Villalon, E., and W. J. Burke, Diffusion of radiation belt protons by whistler waves, *J. Geophys. Res., 99*, 21329, 1994.

Wing, S., and D. G. Sibeck, Effects of interplanetary magnetic field z component and the solar wind dynamic pressure on the geosynchronous magnetic field, *J. Geophys. Res., 102*, 7207, 1997.

Figure Captions

Figure 1. The timeseries of spacecraft-measured magnetic compressions in the dayside magnetosphere used to drive the magnetic-pumping computer simulations. Each color is data from one pass of a GOES spacecraft between 10 and 14 hr local time.

Figure 2. A sketch of the two-dimensional p-α grid used for the simulations of compressional magnetic pumping. A typical grid used for the simulations is 2401×91 gridpoints in p and α.

Figure 3. Bounce averaged pitch-angle diffusion coefficients $D_{\alpha\alpha}$ for electrons (in units of radians^2 s^{-1}) in the dayside magnetosphere are plotted as functions of the equatorial pitch angle. In the top panel the solid curves are calculated $D_{\alpha\alpha}$ values for whistler-mode chorus waves from *Horne et al.* [2013] and the dashed curves are algebraic parameterizations of the calculated values. In the bottom panel the solid curves are parameterizations of the $D_{\alpha\alpha}$ values for EMIC waves from Fig. 3c of *Ukhorskiy et al.* [2010].

Figure 4. Six initial-value simulations of compressional magnetic pumping of electrons catalyzed by whistler-chorus pitch-angle scattering. The six dashed curves are the initial energy distributions (isotropic in pitch angle) of electrons in the six simulations and the six solid curves are the electron energy distributions after 1 day of compressional magnetic pumping. The simulation grids were 2401×91 gridpoints in p and α. The atmospheric loss cone was operating in all of the simulations and the plotted curves are integrated over all pitch angles.

Figure 5. Four initial-value simulations of compressional magnetic pumping of electrons catalyzed by EMIC pitch-angle scattering. The four dashed curves are the initial energy distributions (isotropic in pitch angle) of electrons in the four simulations and the four solid curves are the electron energy distributions after 1 day of compressional magnetic pumping. The simula-

tion grids were 3601×91 gridpoints in p and α. The atmospheric loss cone was operating in all of the simulations and the plotted curves are integrated over all pitch angles.

Figure 6. For the initial-value-problem simulations of Figures 5 and 6, the fractional energy gain of the electron distributions after 1 day of compressional magnetic pumping are plotted as a function of the initial energy of the electrons. The blue curve is for whistler-chorus catalyzed magnetic pumping and the green curve is for EMIC-catalyzed magnetic pumping.

Figure 7. For the initial-value-problem simulations of Figures 5 and 6, the loss rate of electrons into the atmospheric loss cone is plotted as a function of time for 1 day of compressional magnetic pumping. The solid curves are for whistler-chorus waves producing the pitch-angle scattering in the simulations and the dashed curves are for EMIC waves producing the pitch-angle scattering in the simulations.

Figure 8. Three boundary-value simulations of compressional magnetic pumping of electrons catalyzed by whistler-chorus pitch-angle scattering. In the boundary-value simulations a constant supply of low-energy electrons in maintained. In the three simulations the maximum energy of the maintained distribution is 50 keV (green curve), 100 keV (orange curve), and 200 keV (light-blue curves). The three solid curves are the electron energy distributions after 1 day of compressional magnetic pumping. The simulation grids were 2401×91 gridpoints in p and α, the atmospheric loss cone was operating in all of the simulations, and the plotted curves are integrated over all pitch angles.

Figure Bounce averaged whistler-chorus energy-diffusion coefficients D_{EE} (top panel) and momentum-diffusion coefficients D_{pp} for electrons in the dayside magnetosphere are plotted as functions of the equatorial pitch angle. The DEE coefficients are calculated in *Horne et al.* [2013] and the D_{pp}

coefficients are calculated from the D_{EE} coefficients.

Figure 10. Initial-value simulations are run for 100-keV electrons (a), 500-keV electrons (b), and 1-MeV electrons (c). The black dashed curves are the initial energy distributions and the solid curves are the distributions after 1 day of chorus-catalyzed magnetic pumping with a 2401×91 grid (blue), after 1 day of EMIC-catalyzed magnetic pumping with a 3601×91 grid (green), and after 1-day of whistler-chorus energy diffusion with a 10001×91 grid (red). The atmospheric loss cone was operating in all of the simulations and the plotted curves are integrated over all pitch angles.

Figure 11. Phase-space densities at fixed energies are examined at 500 keV, 1 MeV, and 2 MeV for electrons starting out at 250 keV, 500 keV, and 1 MeV, respectively in panels (a), (b), and (c). Initial-value simulations are run for for chorus-catalyzed magnetic pumping with a 2401×91 grid (blue curves), for EMIC-catalyzed magnetic pumping with a 3601×91 grid (green curves), and for whistler-chorus energy diffusion with a 10001×91 grid (red curves). The atmospheric loss cone was operating in all of the simulations and the plotted curves are integrated over all pitch angles.

Figure 12. Seven initial-value simulations of compressional magnetic pumping of electrons catalyzed by EMIC pitch-angle scattering. The dashed black curve is the initial energy distribution (isotropic in pitch angle) of electrons in all seven simulations. The seven solid curves are the electron energy distributions after 1 day of compressional magnetic pumping with seven different amplitudes for the EMIC waves. The simulation grids were 3601×91 grid-points in p and α. The atmospheric loss cone was operating in all of the simulations and the plotted curves are integrated over all pitch angles.

Figure 13. In the top panel the superposed epoch average of the 10-minute change in the solar-wind ram pressure ?Pram10 as measured by ACE is plotted. In the bottom panel the superposed epoch average of the 10-minute

change $\Delta B_{10}/B$ in the dayside magnetic-field strength at geosynchronous orbit as measured by the GOES spacecraft is plotted. In both panels the blue curves are for 70 high-speed-stream-driven storms and the red curves are for 47 coronal-mass-ejection (CME) sheaths. The zero epoch for the blue curves is the onset of the high-speed-stream-driven storm and the zero epoch for the red curves is the passage of an interplanetary shock.

Figure 1.

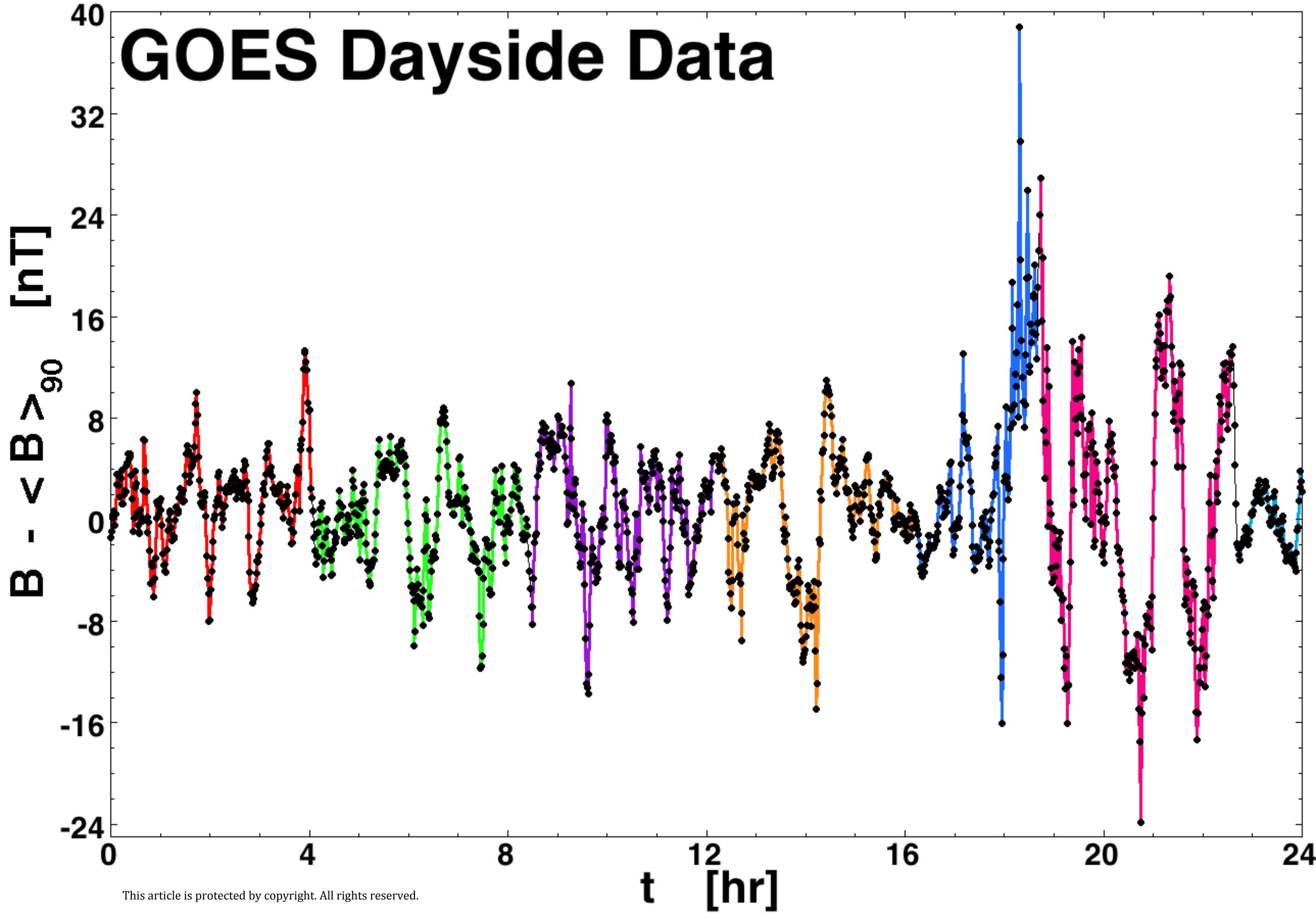

Figure 2.

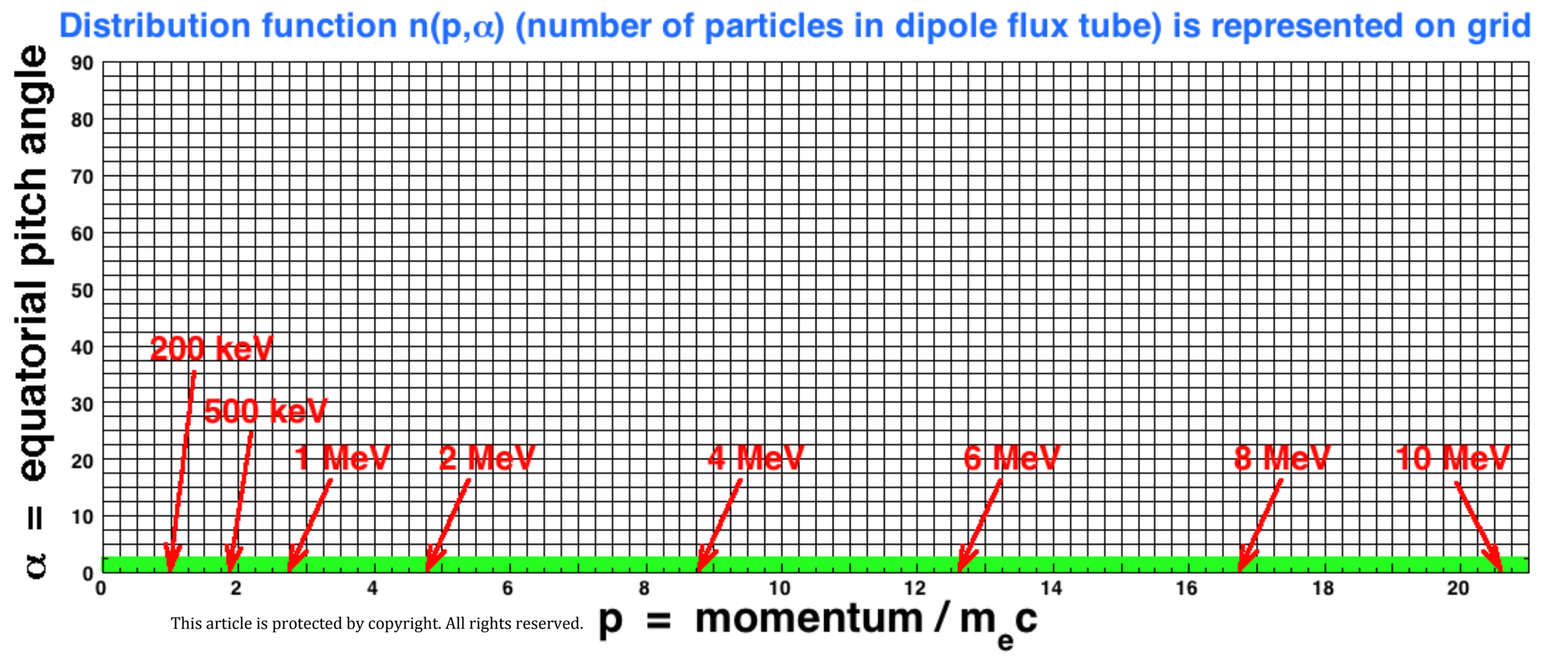

Figure 3.

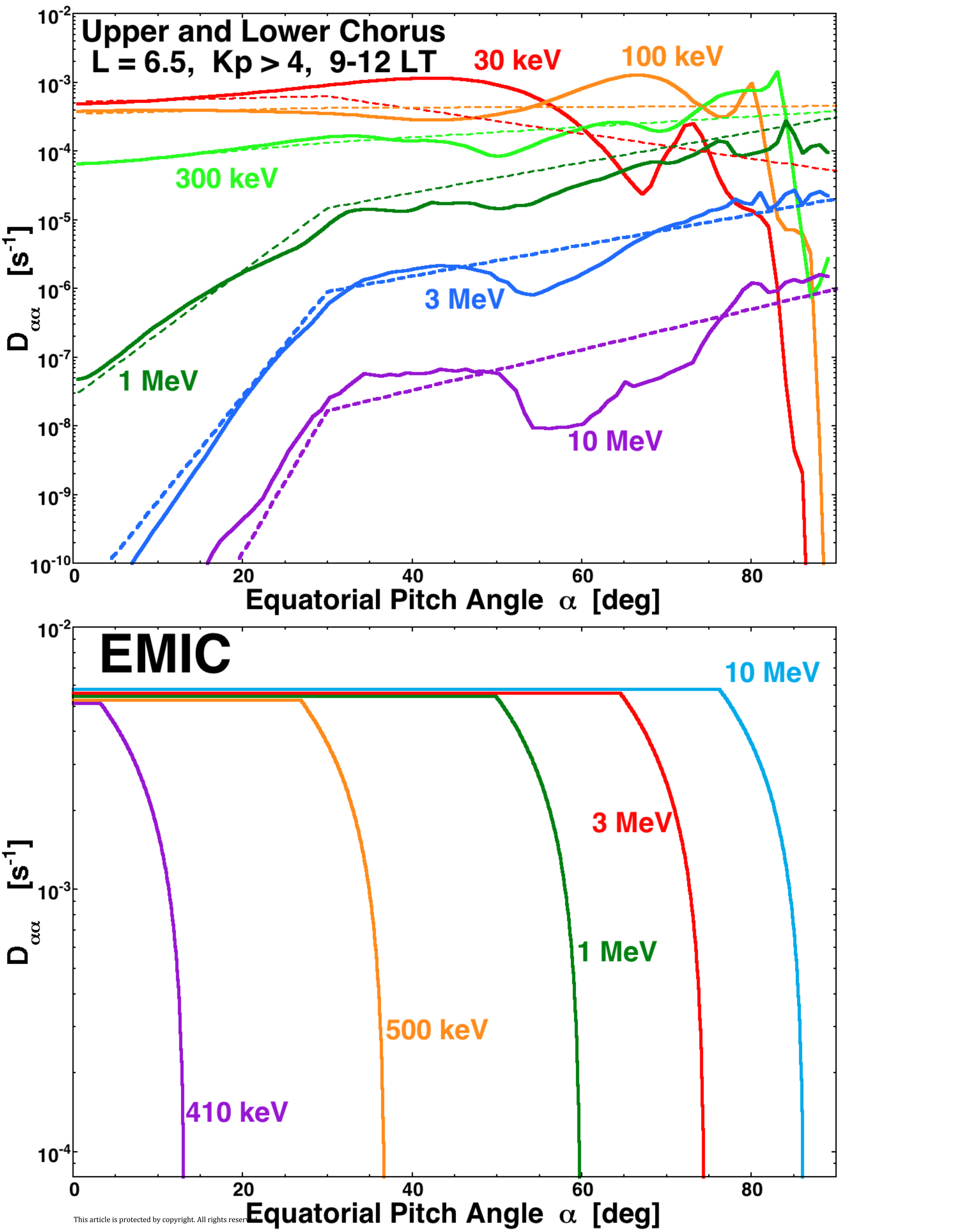

Figure 4.

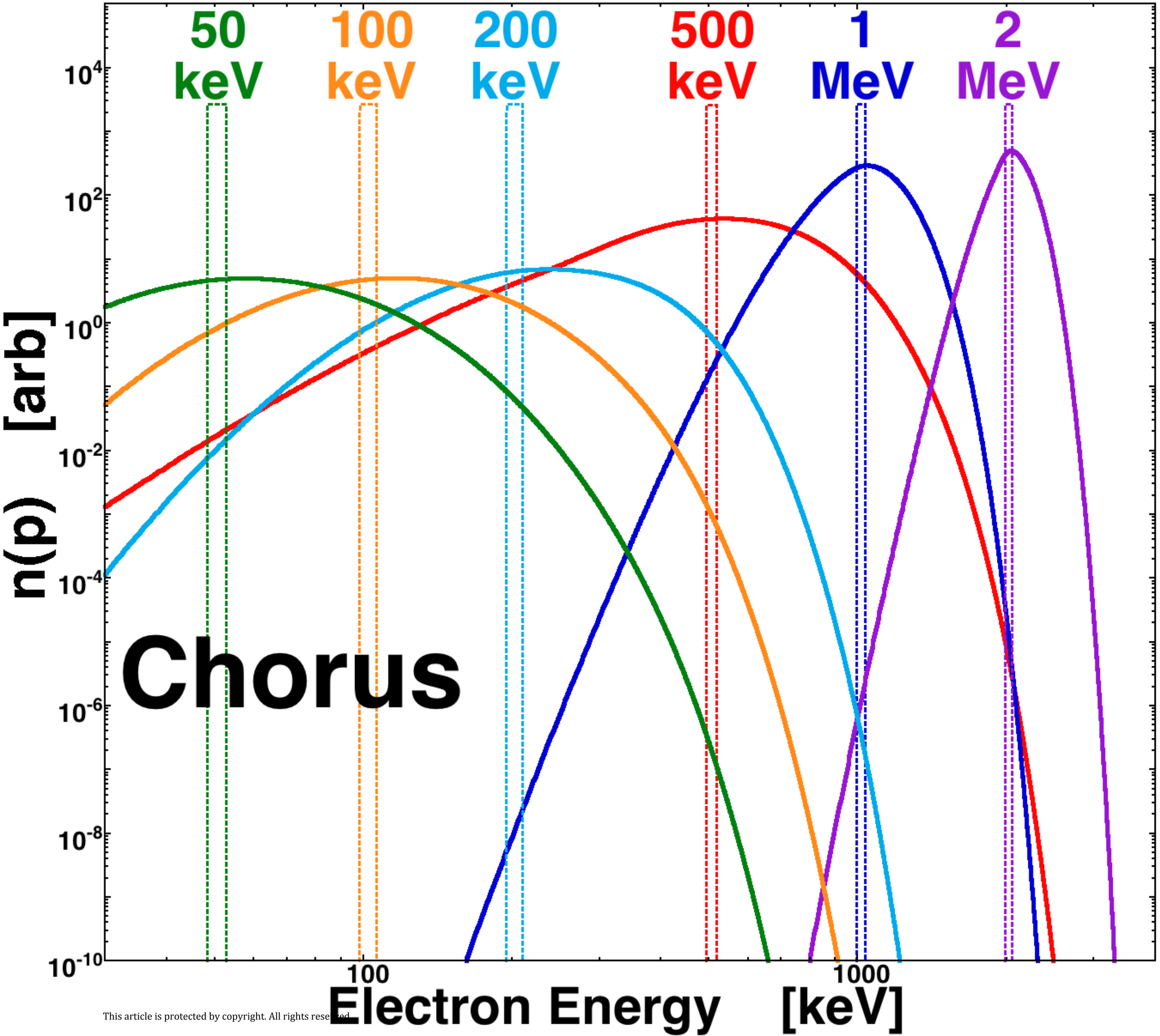

Figure 5.

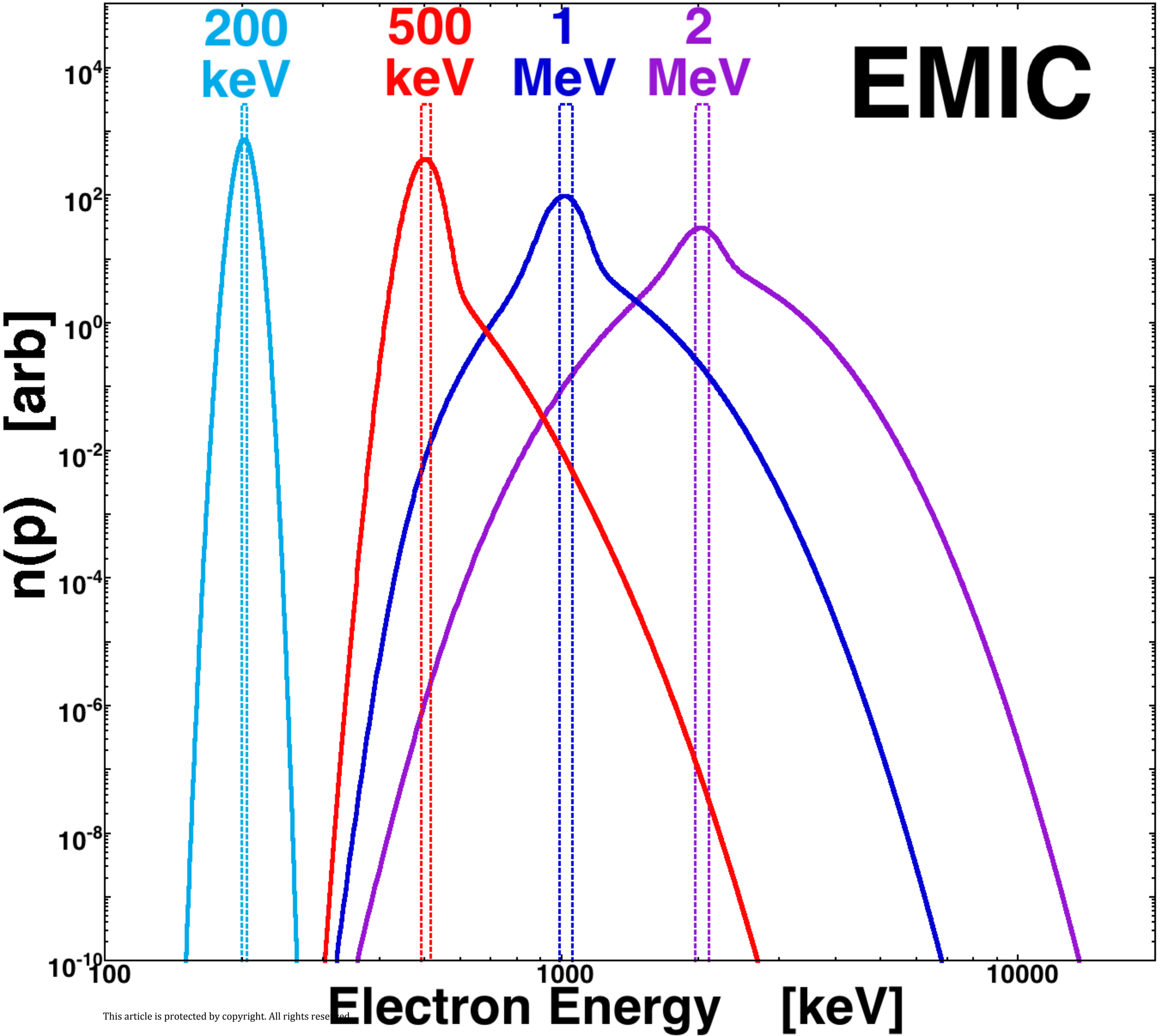

Figure 6.

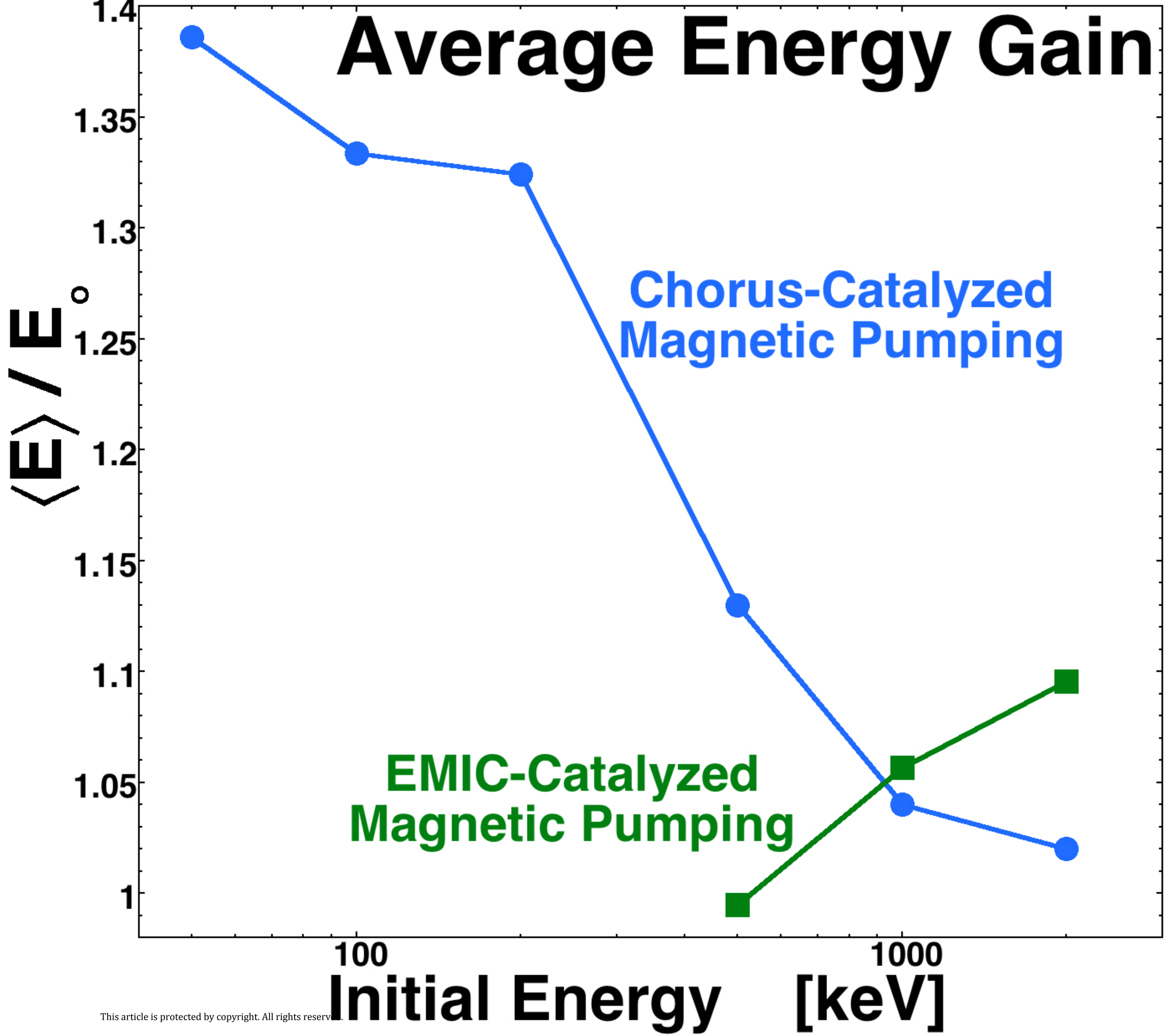

Figure 7.

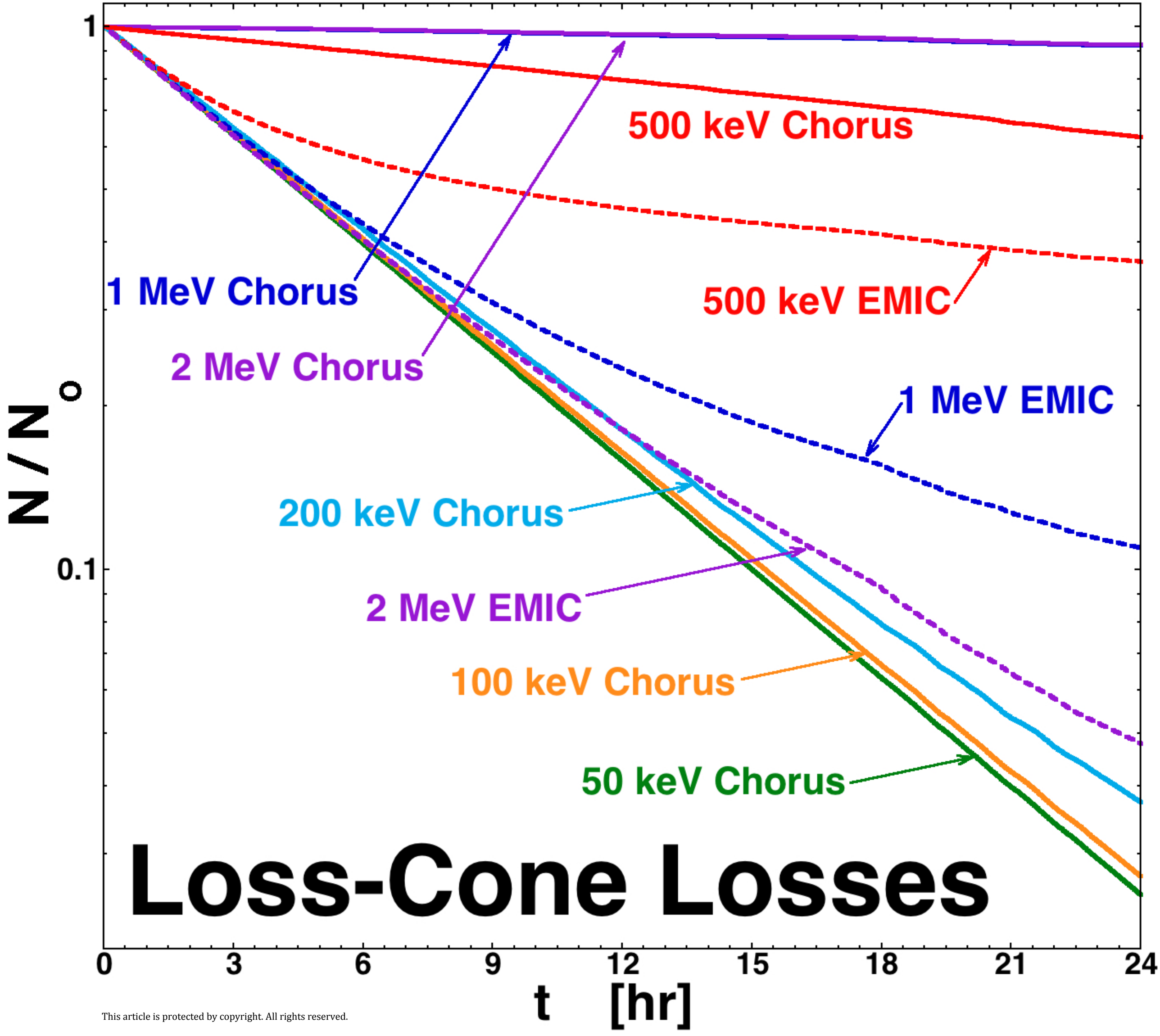

Figure 8.

Chorus

200 keV
6 hr

200 keV
24 hr

200 keV
1 hr

100 keV
24 hr

50 keV
24 hr

n(p) [arb]

10^{2}
10^{0}
10^{-2}
10^{-4}
10^{-6}
10^{-8}
10^{-10}

0
200
400
600
800
1000
1200

Electron Energy [keV]

Figure 9.

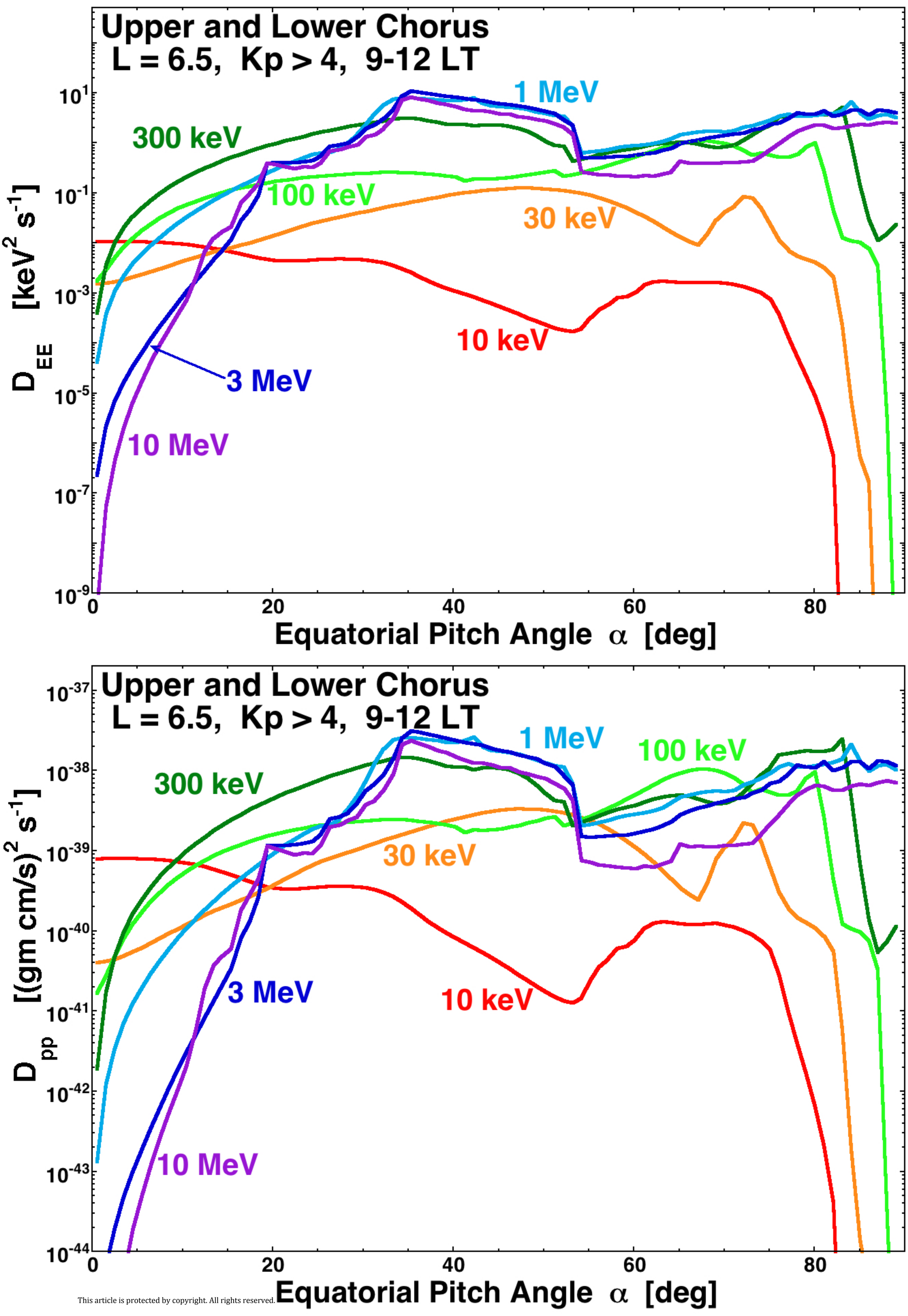

Figure 10.

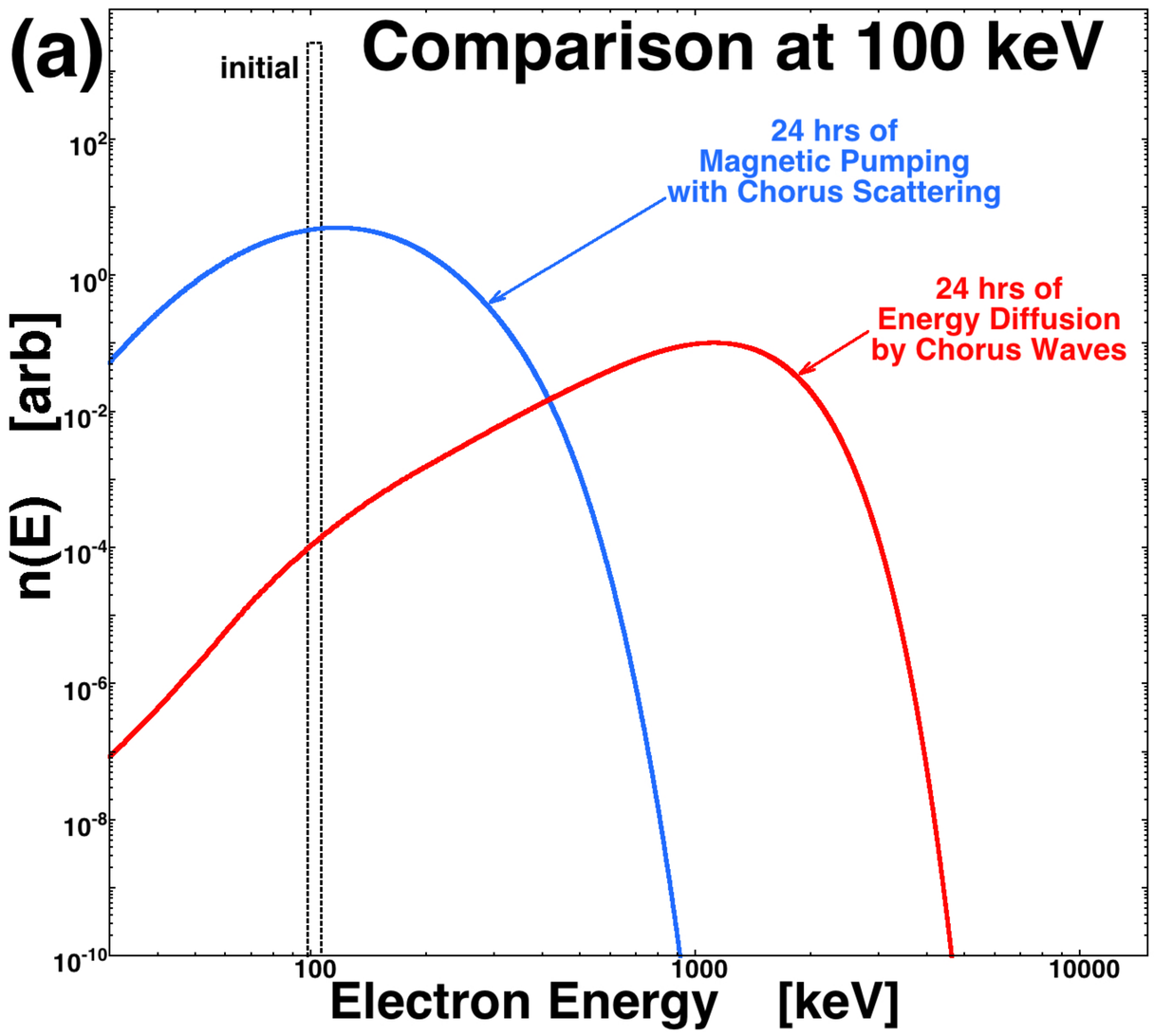

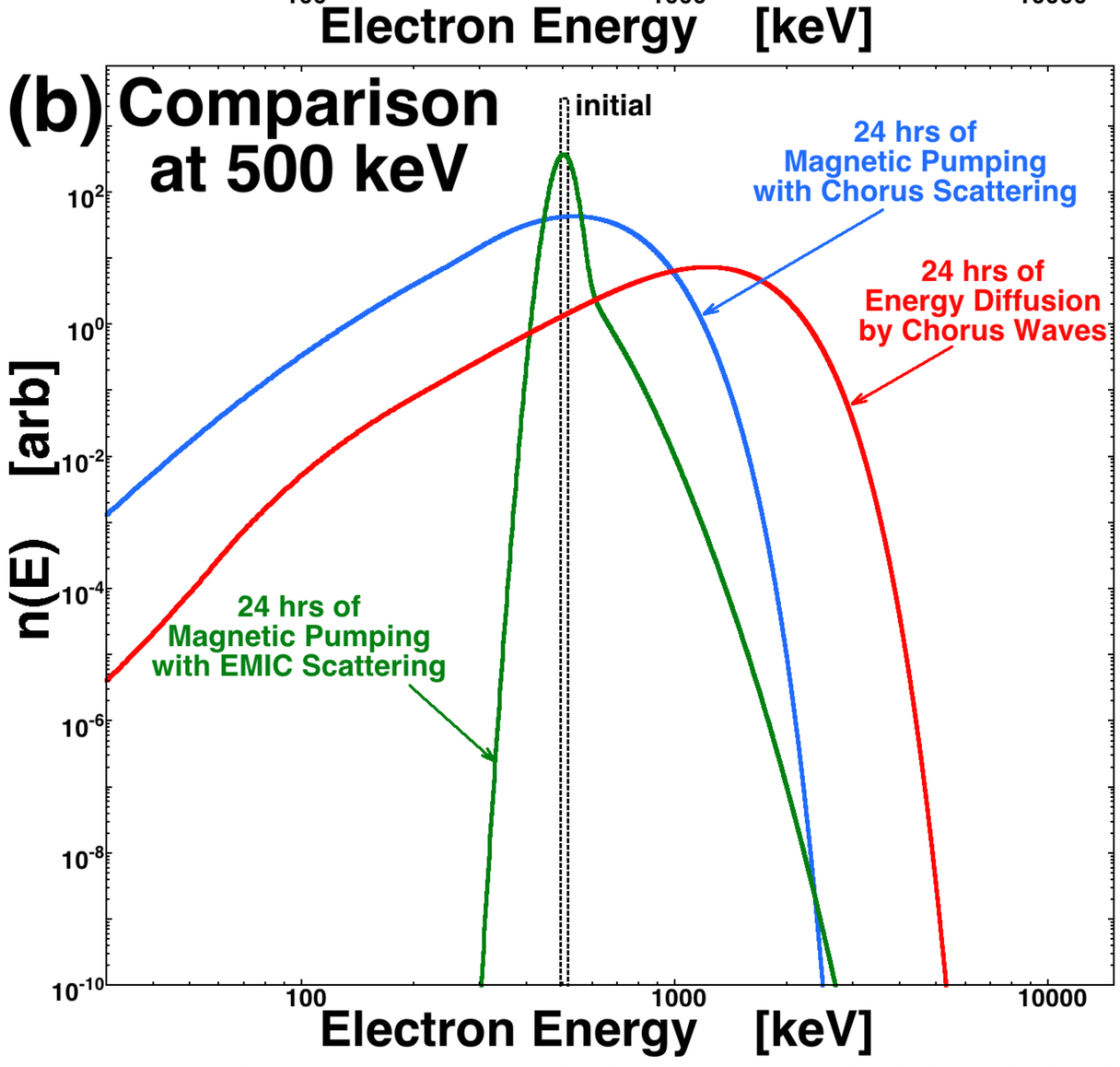

Figure 11.

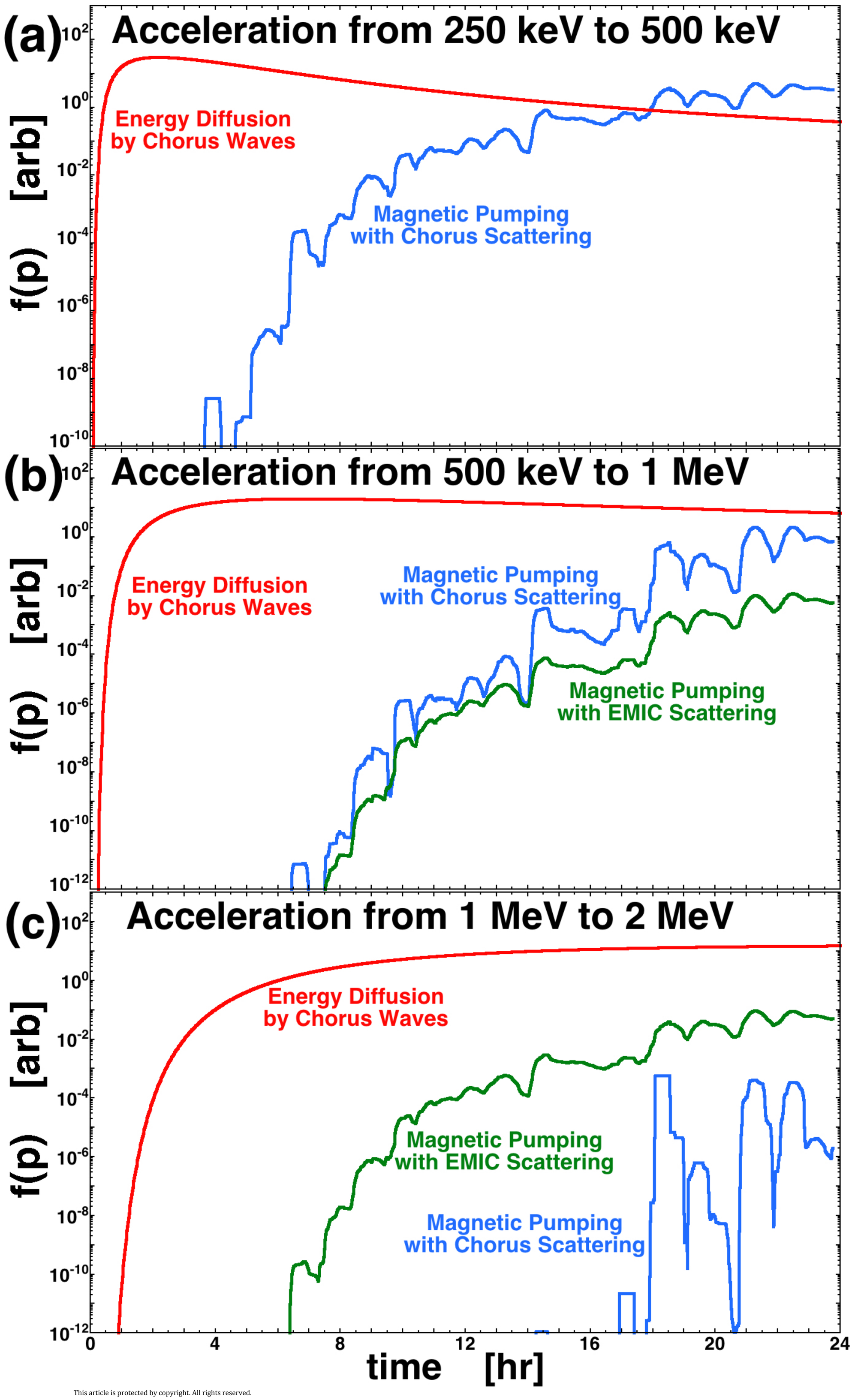

Figure 12.

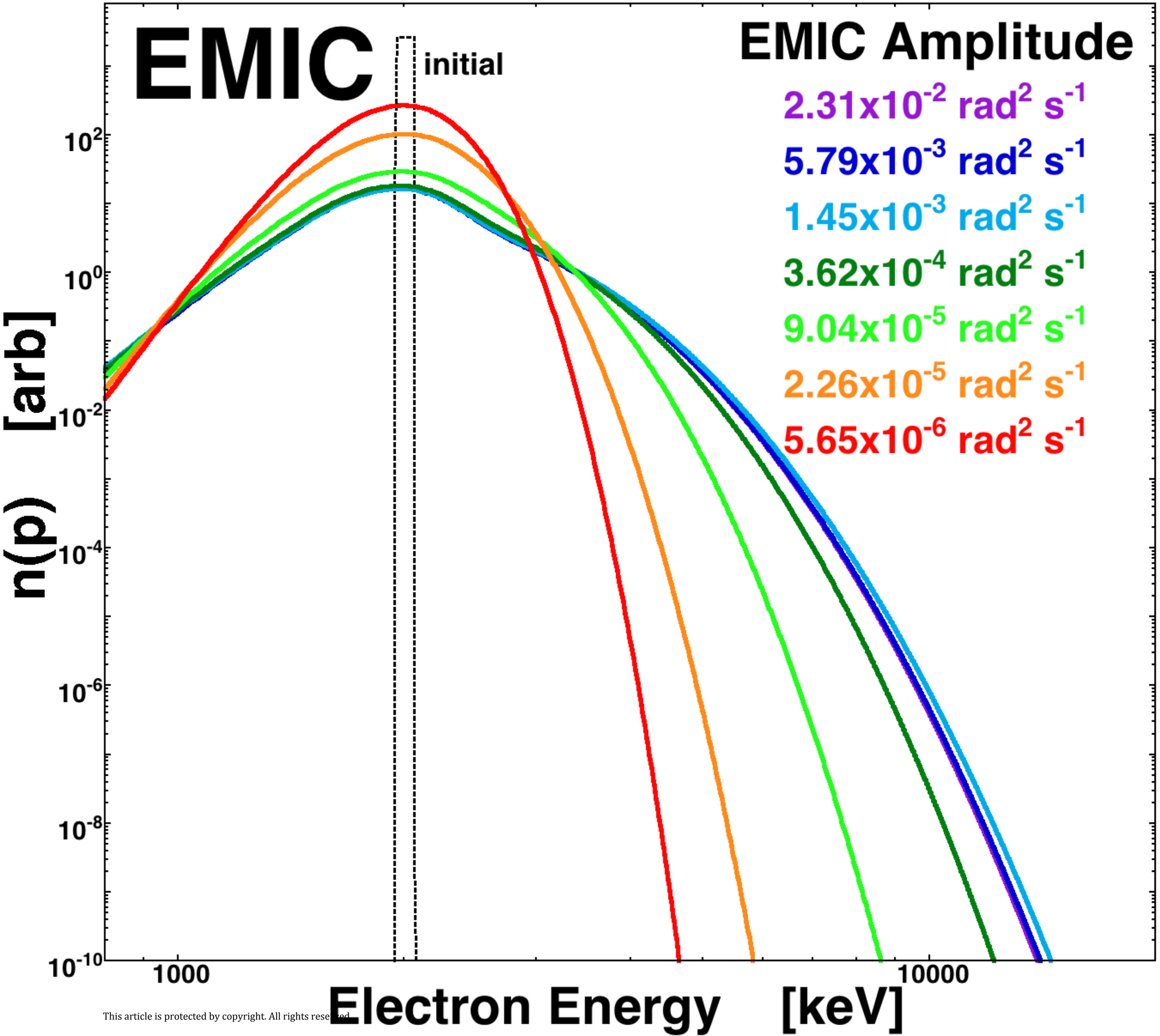

Figure 13.